JGR Solid Earth

RESEARCH ARTICLE
10.1029/2020JB019509

Key Points:
- Mylonitic and ultramylonitic domains are enriched in Cl-bearing Mg-hornblende (Mg-Hbl)
- Synkinematic Mg-hornblende was formed between 800°C and 850°C
- Mg-Hbl mylonites can be the geological expression of microseismicity in mid-ocean ridges and act as fluid pathways along detachment faults

Supporting Information:
- Supporting Information S1
- Figure S3
- Data Set S1
- Data Set S2
- Data Set S3
- Data Set S4
- Data Set S5

Correspondence to:
J. F. Vieira Duarte,
joana.vieira@geo.unibe.ch

Citation:
Vieira Duarte, J. F., Kaczmarek, M.-A., Vonlanthen, P., Putlitz, B., & Müntener, O. (2020). Hydration of a mantle shear zone beyond serpentine stability: A possible link to microseismicity along ultraslow spreading ridges? *Journal of Geophysical Research: Solid Earth*, *125*, e2020JB019509. https://doi.org/10.1029/2020JB019509

Received 31 JAN 2020
Accepted 25 SEP 2020
Accepted article online 12 OCT 2020

Hydration of a Mantle Shear Zone Beyond Serpentine Stability: A Possible Link to Microseismicity Along Ultraslow Spreading Ridges?

J. F. Vieira Duarte[1,2], M.-A. Kaczmarek[1,3], P. Vonlanthen[1], B. Putlitz[1], and O. Müntener[1]

[1]Institute of Earth Sciences, UNIL-Mouline, University of Lausanne, Lausanne, Switzerland, [2]Institute of Geological Sciences, University of Bern, Bern, Switzerland, [3]Géosciences Environnement Toulouse (GET), CNRS-CNES-IRD-Université de Toulouse III, Observatoire Midi Pyrénées, Toulouse, France

Abstract Hydration of the oceanic mantle is a fundamental process of the global water cycle promoting chemical and volumetric changes and facilitating mantle exhumation along detachment faults. At which depth these processes occur and how fluids circulate along ductile mantle shear zones are, however, less well constrained. Here we present field, chemical, and microstructural evidence of hydration processes of peridotite mylonites within an upper mantle shear zone from an Alpine ophiolite (Lanzo massif, Italy). Mylonitic and ultramylonitic areas of the anastomosing shear zone are enriched in Cl-bearing amphibole. Electron backscatter diffraction (EBSD) data indicate the activation of the (100)[001] amphibole slip system arguing for synkinematic growth and deformation at temperatures consistent with Mg-hornblende stability between 800°C and 850°C. High Cl contents in amphibole (0.15–0.61 wt%) as well as oxygen isotope data ($\delta^{18}O_{whole\text{-}rock}$ between 4.4‰ and 4.7‰) indicate accumulation and focusing of seawater-derived fluid in mylonitic and ultramylonitic domains. Such hydration processes are consistent with strain partitioning between water-poor (less deformed) and water-rich (intensely deformed) layers, consistent with changes in olivine and pyroxene crystallographic preferred orientations (CPOs). Our results support recent geophysical data from ultraslow spreading mid-ocean ridge systems that fluids might penetrate beyond the stability of serpentine to depth between 6 and 15 km. Such peridotite shear zones act as fluid pathways for long-lived detachment faults or oceanic transform faults, along which upper mantle rocks are exhumed to the seafloor. Fracturing and fluid flow along such peridotite shear zones might be recorded by deep microseismicity along ultraslow spreading ridges.

1. Introduction

The hydration of exhumed mantle along detachment faults or oceanic transform faults is a fundamental process of the near-seafloor hydrological cycle. Since the discovery of exhumed mantle offshore Iberia (Boillot et al., 1989), along mid-ocean ridges (e.g., Bonatti, 1968) in oceanic core complexes (e.g., Tucholke et al., 1998) and oceanic transform faults (e.g., Jaroslow et al., 1996), a fundamental question is how fluid circulation and faulting interact beneath the seafloor. The extent of mantle hydration (i.e., serpentinization) away from ultraslow spreading ridges is generally believed to be restricted to the brittle regime and temperatures not exceeding 600°C (e.g., McKenzie et al., 2005). Significant mantle hydration or serpentinization generally occurs at depth shallower than about 3 km (Minshull et al., 1998; Skelton et al., 2005) passively at the ocean floor (serpentinization), or through brittle faults that control the migration of fluids by providing structural conduits and seismic pumping (Sibson et al., 1975). Seismic studies indicate that serpentinization is decreasing with depth and probably becomes insignificant at depths exceeding ~5–6 km below the seafloor (e.g., Minshull, 2009; Minshull et al., 1998). Seismic data indicate that serpentinization correlates with fault displacement during continental rifting (Bayrakci et al., 2016). Recent studies using a dense network of ocean bottom seismometers have challenged the ideas about the strength of the mantle lithosphere at ultraslow spreading ridges and have shown that microseismicity might occur at depth of 6–13 or even 20 km (Grevemeyer et al., 2019; Parnell-Turner et al., 2017; Schlindwein & Schmid, 2016; Yu et al., 2018). This indicates, at least episodically, semibrittle behavior of the oceanic lithosphere along ultraslow spreading ridges. However, the maximum depth at which hydration of mantle rocks occur and fluids can penetrate through mantle shear zones is poorly constrained.

Peridotite mylonites represent direct evidence of strain localization in upper mantle shear zones. Such structures are considered to play an important role for exhumation of mantle rocks to the ocean floor, specifically along transform faults and (ultraslow) slow spreading ridges (Bonatti, 1990; Cannat, 1993; Jaroslow et al., 1996; Seyler & Bonatti, 1997; Tucholke et al., 2001). Peridotite mylonites are mechanically weak zones that develop at the expense of coarser-grained mantle rocks. Therefore, they may exert an important control on the strength and deformation processes of mantle lithosphere, from continental rifting to oceanic-continent transition zones (OCTs) and oceanic core complex formation (e.g., Cannat & Sauter, 2009; Dijkstra et al., 2002; Ildefonse et al., 2007; Kaczmarek & Tommasi, 2011; Précigout et al., 2017; Vissers et al., 1995; Warren & Hirth, 2006).

Weakening of mantle peridotite and the localization of deformation are enhanced by the combined effects of grain size reduction through dynamic recrystallization (Braun et al., 1999), melt-rock reaction and mechanical mixing of mineral phases (Dijkstra et al., 2002), change in the dominant creep mechanism (Drury & Urai, 1990), subsolidus metamorphic reactions (Newman et al., 1999), shear heating (Regenauer-Lieb & Yuen, 2003), pinning by secondary phases (Linckens et al., 2011), and intrinsic anisotropy of constituent crystals (Bai et al., 1991; Durham & Goetze, 1977; Tommasi et al., 2009). Among these processes, thermal gradients (Précigout et al., 2017; Soustelle et al., 2009; Vissers et al., 1995) and the presence of melt and/or fluids (e.g., Albers et al., 2019; Brown & Solar, 1999; Holtzman & Kohlstedt, 2007; Kelemen et al., 1995; Le Roux et al., 2008; Tommasi et al., 1994) are fundamental parameters controlling the rheology of the upper mantle. Hirth and Kohlstedt (1995) showed that very low melt fractions ($\leq$1%) can lower the yield strength in solid-state flow and viscosity by more than 1 order of magnitude (Rosenberg & Handy, 2000; Takei, 2005), promoting recrystallization and grain growth. In contrast, deformation itself may enhance permeability and lead to focusing of mobile components such as fluids or melts into anastomosing shear bands or channels (Holtzman et al., 2003; Holtzman & Kohlstedt, 2007; Kaczmarek & Müntener, 2008; Kelemen et al., 1995; Kohlstedt & Holtzman, 2009; Précigout et al., 2017). At deeper levels, in a ductile regime, different mechanisms are likely to occur in shear zones: transient fracturing events, porosity increase caused by grain size reduction (Wark & Watson, 2000), or cavitation creep/dynamic pumping through opening of microcavities (Fusseis et al., 2009; Précigout et al., 2017). Evidence for the latter process was reported from the Ronda Massif peridotite mylonites in Spain, where syntectonic water infiltration is documented by amphibole enrichment and changes in the fabric and dislocation slip system of olivine (Précigout et al., 2017).

In this study, we present field and microstructural evidence of hydration processes beyond serpentine stability, in peridotite mylonites from the Lanzo massif (Italian Alps). In this massif a km-scale mantle shear zone with traces of hydration is exposed and been interpreted as an analog for peridotite mylonites along ultraslow spreading ridges (Kaczmarek & Müntener, 2008). Hydration is identified by enrichments of amphibole in the shear zone and a change in olivine crystallographic preferred orientation (CPO) in mylonites. We combine electron backscatter diffraction (EBSD) studies on amphibole, clinopyroxene, orthopyroxene, and olivine with mineral chemical data to constrain the formation conditions of amphibole in the hydrous mylonite zone. Chlorine contents in amphibole as well as oxygen isotope data indicate accumulation and focusing of seawater-derived fluid flow in the mylonitic and ultramylonitic domains. Our results show that fluids might penetrate down to depths of 10–15 km, beyond serpentine stability, supporting recent geophysical data. Therefore, amphibole-bearing mantle mylonite zones provide important constraints on the depth of hydration of upper mantle rocks in the oceanic crust.

2. Geological Setting

The Lanzo massif is located in northwestern Italy (Figure 1) and forms part of a large belt of ophiolites interpreted as remnants of the former Piemonte-Ligurian Ocean (Pognante et al., 1985). To the west, it is delimited from the Piemontese ophiolites and Mesozoic metasediments by the "Viu Locana" zone, and to the east, from the Po basin by the Insubric Line (Nicolas, 1974; Pognante, 1989; Spalla et al., 1983). The Lanzo massif is mainly composed of coarse-grained porphyroclastic plagioclase lherzolites (with minor spinel lherzolites, pyroxenites, and dunites, surrounded and partially overprinted by serpentinites). Two NW-striking, km-scale, shear zones crosscut the entire massif, one in the north (separating the central and northern Lanzo domains, and called northern shear zone hereafter) and one in the south (Boudier, 1978). Detailed petrographic and structural studies of the northern shear zone highlight an asymmetric distribution of the

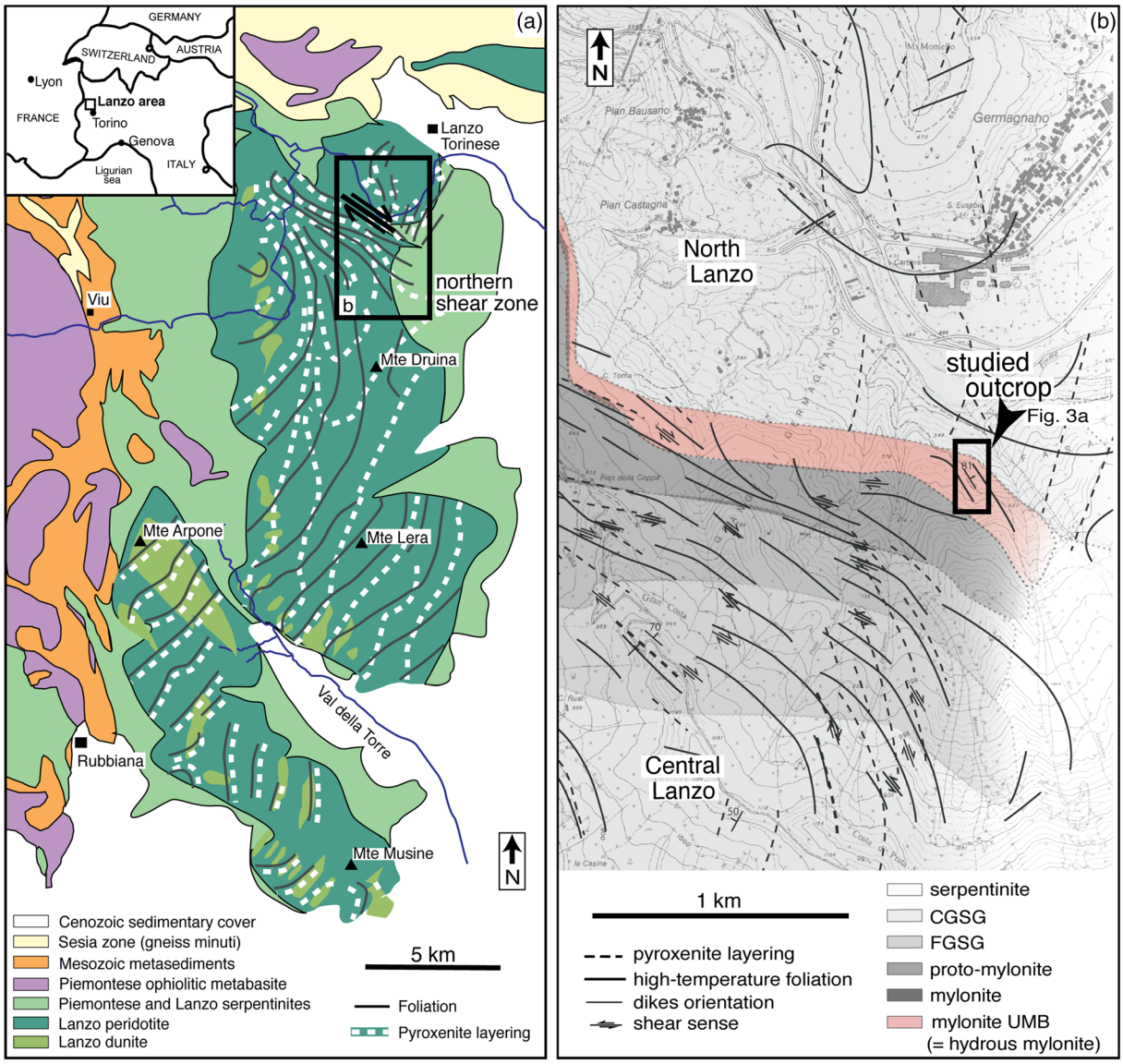

Figure 1. Location of the peridotite mylonites. (a) Geological map of the Lanzo massif (modified from Boudier, 1978). The northern shear zone shown in (b) is indicated by a square. (b) Structural map of the northern shear zone (modified from Kaczmarek & Müntener, 2008). CGSG and FGSG are for coarse and fine grain secondary granular peridotite, respectively. The studied outcrop focuses on the mylonites containing ultramylonitic bands (UMB) and is referred to as hydrous mylonite zone (see Figure 2a for details).

deformation gradient (Kaczmarek & Müntener, 2008; Kaczmarek & Tommasi, 2011). From south to north, the grain size progressively decreases within the shear zone and the main foliation becomes subparallel to the contact with the northern domain. The northern boundary of the shear zone is defined by a sharp transition between a ~100 m wide domain composed by an anastomosing network of peridotite mylonite with amphibole-bearing mm-scale ultramylonitic bands and coarse-grained peridotites of the northern Lanzo domain (Kaczmarek & Tommasi, 2011). The northern shear zone has been interpreted as a result of mantle exhumation related to the opening of the Piemonte-Ligurian Ocean (Lagabrielle & Lemoine, 1997; Lemoine et al., 1987).

Spinel and pyroxene mineral chemistry combined with preserved melt-rock reaction textures and orthopyroxene diffusion profiles indicate rapid exhumation of the Lanzo massif (Jollands & Müntener, 2019). Al-rich pyroxene cores in equilibrium with spinel indicate equilibration temperatures of 1100–1030°C, whereas Al-poor recrystallized pyroxenes in equilibrium with plagioclase gave lower equilibration temperatures of

Table 1
List of the Samples Analyzed According to the Nomenclature of Vernon (2018), Together With Their Mg-Hornblende (Mg-Hbl) Modal Abundance

Sample microtexture	Lithology[a]	Mg-Hbl (vol%)	Sample
Protogranular	Lherzolite	2	La02
	Hbl-rich vein	98	La37
	Harzburgite	2	La38
	Lherzolite	3	La23
Protomylonite	Gabbro	35	La06
	Gabbro	35	La08
	Lherzolite	5	La10
	Olivine websterite	3	La11
	Lherzolite	8	La14
	Olivine websterite	4	La22
	Olivine websterite	5	La29
	Lherzolite	2	La13
	Lherzolite	2	La35
Mylonite	Lherzolite	7	La03
	Lherzolite	15	La04
	Harzburgite	5	La17
	Lherzolite with gabbro veinlet	30	La20
	Olivine websterite	9	La24
	Pyroxenite serpentinized	0	La36
Mylonite/ ultramylonite	Olivine websterite	5	La19
	Lherzolite	7	La21
Ultramylonite	Lherzolite/Opx websterite	10	La18
	Lherzolite	2[b]	La32
	Lherzolite	2[b]	La34

Note. For each microtexture, samples are listed from north to south. Note that sample microtexture is variable at mm scale and therefore can be attributed to a different microtextural domain on a larger scale (see Figure 2 for specific sampling locations). For simplification general peridotite and pyroxenite terminology was used in the text.
[a]Peridotitic rocks include lherzolite and harzburgite; pyroxenitic rocks include olivine websterite and Opx websterite. [b]Not taking kaersutite, ~8 vol%, into account.

about ~850°C (Kaczmarek & Müntener, 2008). Grain size reduction coupled to temperature decrease indicates progressive strain localization that led ultimately to the formation of mylonites and ultramylonites from precursor coarse-grained peridotites (Kaczmarek & Tommasi, 2011). Using the forsterite-anorthite Ca-Tschermak enstatite (FACE) geobarometer for plagioclase peridotite mylonites (Fumagalli et al., 2017), pressure conditions have been estimated at 0.3–0.5 GPa, which constrains the maximum depth of fluid infiltration required for amphibole formation to about 10–15 km. The absence of gabbro dikes in the hanging wall (northern body) of the northern shear zone, along with the presence of plagioclase-rich lenses and amphibole-gabbro dikelets in the hydrous mylonite zone, indicate that the actively deforming shear zone was impermeable for migrating gabbroic dikes and fluids (Kaczmarek, 2007; Kaczmarek & Müntener, 2008).

3. Methods

This study focuses on the hydrous mylonite zone of the Lanzo northern shear zone (Kaczmarek & Müntener, 2008). Forty-four mafic and ultramafic samples were collected along a ~200 m long transect oriented normal to the shear zone (Figure 1). Field observations were complemented by chemical, isotopic, and EBSD analyses, all conducted at the University of Lausanne (Switzerland). A list of the samples analyzed in the laboratory, containing lithological and microtextural information, is available in Table 1, and corresponding sampling locations are shown in Figure 2.

In situ chemical compositions of olivine, orthopyroxene, clinopyroxene, spinel, and amphibole from different rock types and textures were measured in 13 samples. A JEOL JXA-8200 electron probe micro-analyzer (EPMA) has been used, which was equipped with five wavelength-dispersive spectrometers (WDSs) and operated at an acceleration voltage of 15 kV and a probe current of 15 nA. X-ray intensities and peak-to-background ratios were measured for major elements from Kα and Lα lines using a combination of LIF, PET, TAP, and LDE crystals for better sensitivity and counting statistics. The detection limit ranged between 0.01 and 0.05 wt% for all major elements. Automated matrix correction was achieved following the ϕρz procedure. The results were then compared with data collected in the Lanzo northern shear zone (Kaczmarek & Müntener, 2008), abyssal spinel peridotites (Hellebrand et al., 2002), and ultramafic mylonitic rocks from the Ronda massif (Hidas et al., 2016; Précigout et al., 2017), Cabo Ortegal (Tilhac et al., 2016), transform faults in the Vema transect in the Mid-Atlantic Ridge (Cipriani et al., 2009), and in the Southwest Indian Ridge (SWIR; Prigent et al., 2020).

The oxygen isotope composition of whole rocks (six samples) and one amphibole mineral separate were determined at the stable isotope laboratory (University of Lausanne) using the CO_2-laser fluorination technique. The analytical protocol followed the method initially described by Sharp (1990); for further details on the procedure, see Lacroix and Vennemann (2015). Between 1.5 and 2.0 mg of sample material was used. The data were corrected to the session value of the LS-1 quartz, the in-house reference material (accepted value of 18.1‰), and given in conventional δ-notation, relative to Vienna Standard Mean Ocean Water (VSMOW). Duplicate analyses of the LS-1 quartz during this single session yield 18.0 ± 0.08‰ (SD = standard deviation). Duplicate analyses of the amphibole separate (La37) yields 5.5 ± 0.15‰ (SD).

Thin sections perpendicular to the foliation plane and parallel to the lineation were prepared for detailed crystallographic analysis using EBSD. Sample surface preparation included stepwise diamond polishing followed by a 30–45 min chemomechanical polishing step in a suspension of 25 nm colloidal silica (pH 9.8) to eliminate any mechanical damage. No carbon coating was applied in order to guarantee optimum EBSD pattern quality. Data were acquired using a Tescan Mira II LMU field-emission scanning electron microscope

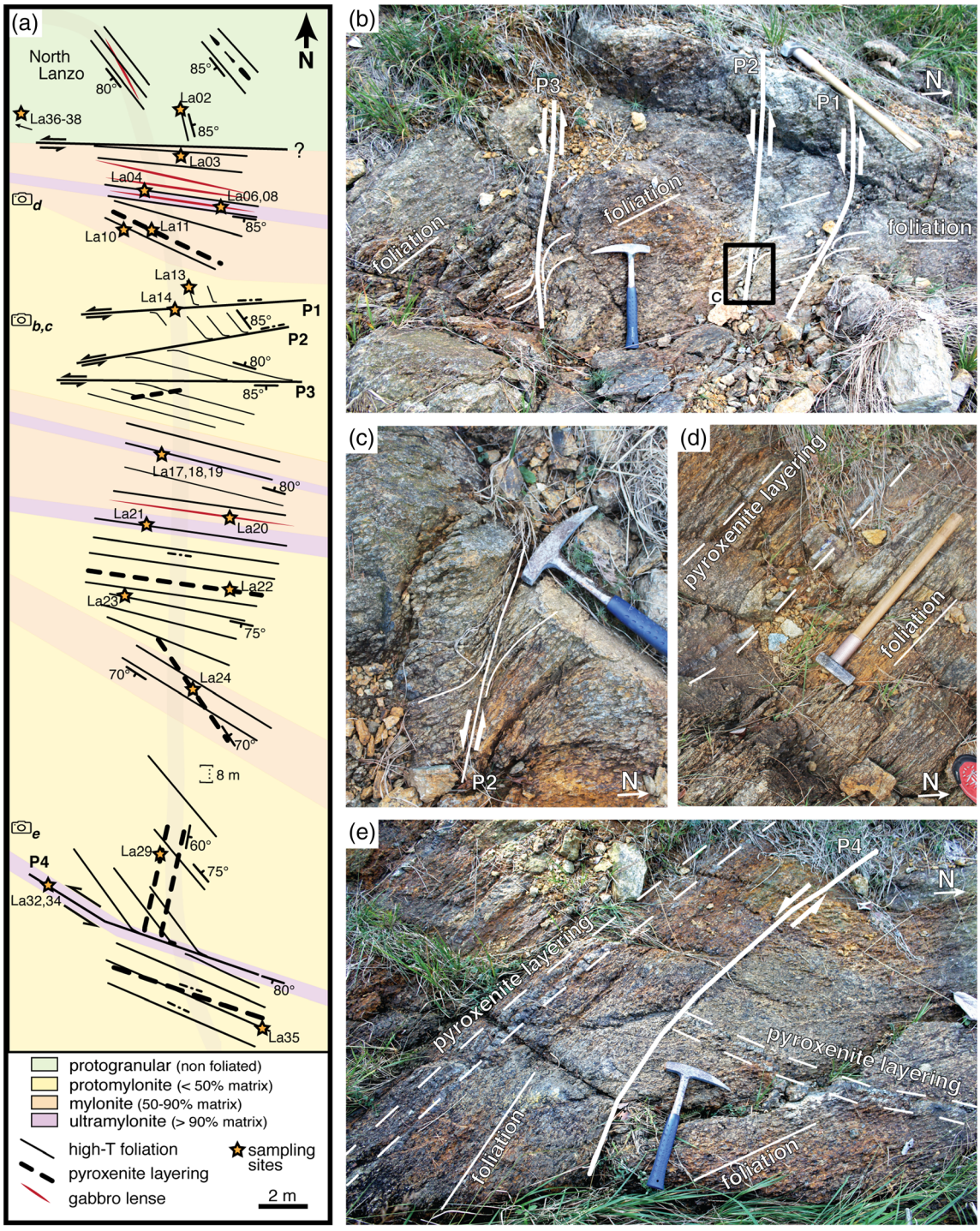

Figure 2. Geological map and structures of the hydrous mylonite zone. (a) Detailed structural map of the selected outcrop (~50 m long), with reference to the different textural types. Shear senses are indicated by arrows. The boundary between the northern and central Lanzo domains is possibly defined by the fault delimiting the protogranular and mylonitic textures at the top of the map. Sampling sites are indicated by yellow stars, and sample description is available in Table 1. (b) Late shear planes affecting the protomylonitic peridotite (P1–P3). (c) Drag fold associated with shear plane P2. (d) Mylonite showing the subparallel relationship between pyroxenite bands and high-temperature foliation. (e) Discordant pyroxenite bands and high-temperature foliation on either side of shear plane P4. Drag folds associated with P4 are only 1 cm in size.

(FE-SEM) equipped with the Nordlys S EBSD camera commercialized by Oxford Instruments. The microscope working conditions were the same for all the maps, with an acceleration voltage of 20 kV, a probe current of ~1.1 nA, a stage tilt of 70°, and a working distance of 23 mm. Automatic indexing of the EBSD patterns was achieved on 10 samples (21 detailed maps) using the AZtec 2.4 software, with step size varying from 0.15 to 30 μm depending on grain sizes and goals. Processing and representation of EBSD data were generated using the MATLAB toolbox MTEX (Bachmann et al., 2010), together with the script developed by Henry et al. (2017). For consistency, a similar procedure was applied to the data published by Kaczmarek and Tommasi (2011). Measurements with a mean angular deviation (MAD) greater than 1.3 were removed, and neighboring measurements with misorientations <10° were considered parts of the same grain. The "splineFilter" function was used to smooth grains and interpolate the missing measurements, and grains smaller than three pixels were removed to avoid bias caused by potential indexing errors. EBSD orientation maps were compared with band contrast maps to ensure that postprocessing did not compromise the quality of the data. The orientation of the crystallographic axes [100], [010], and [001] was projected into lower-hemisphere equal-area pole figures. In order to avoid overrepresentation of large grains and to allow for comparison between fabrics generated from different maps, only one point per grain was plotted in the pole figures. Orientation distribution functions (ODFs) were calculated using a Gaussian half width of 10°, provided that the number of grains was statistically significant (>100). The strength of the CPO was calculated using the J-index (Bunge, 1982) and the M-index (Skemer et al., 2005).

4. Results

4.1. Field and Petrological Observations

The hydrous mylonite zone is mainly constituted of peridotite (lherzolite and minor harzburgite), along with gabbro, and pyroxenite (orthopyroxenite and websterite) (Table 1). The overall paragenesis is composed of olivine, orthopyroxene, clinopyroxene, Cr-spinel surrounded by plagioclase rims, and amphibole. Deformation is highly heterogeneous, with textures varying from protogranular to protomylonitic, mylonitic, and ultramylonitic within a few meters or less. Along the studied transect in the hydrous mylonite zone, strain is further localized into four shear planes up to 1 cm thick (labeled P1 to P4 from north to south in Figure 2e), some of which (P4 in particular) are characterized by a very fine-grained, ultramylonitic matrix with embedded rounded porphyroclasts (Sample La32). Shear planes are associated with incipient cm-scale drag folds (Figures 2b and 2c), suggesting sinistral sense of shear (top to SW). They have been interpreted as of the C′-type following the nomenclature of Platt and Vissers (1980) and are thought to have developed during a later stage of the shear zone history characterized by intense flow partitioning (Kaczmarek, 2007).

The hydrous mylonite zone crosscuts the high-temperature foliation and pyroxenite layering showing orientations oscillating between N85–N160 and N20–N110, respectively. The geometrical relationship between high-temperature foliation and pyroxenite layering can abruptly change from subparallel to discordant, as it is the case when crossing P4 from south to north (Figure 2e). In this zone, evidence of melt and fluid percolation can be observed: numerous millimetric or centimetric gabbroic sills mostly mylonitized, which could contain large phenocrystals of amphibole (Figure 3a), pyroxenite dikelets parallel to the foliation (Figures 2d and 3b), and several cm thick veins rich in Mg-hornblende crosscutting the foliation (Figures 3d–3f).

In the protogranular and protomylonite samples, olivine takes the form of extensively fractured grains, of ~1 cm in size, showing a weak shape preferred orientation. The transition from protomylonitic to mylonitic and ultramylonitic textures is accompanied by an increase in the proportion of the ultramylonitic matrix, shown by a decrease in the grain size of olivine and pyroxene porphyroclasts (ranging from 20 μm up to 1 mm), and increasing shape preferred orientation of the minerals parallel to the lineation. The protomylonite samples show an anastomosing network of fine-grained olivine (0.3 mm in size) defining the foliation, as a consequence of dynamic recrystallization along grain boundaries. Mineral modal abundances show abrupt changes (Figure 4) depending on the mineralogy of the protolith and the degree of deformation. In peridotites, olivine, orthopyroxene, and clinopyroxene react with fluids to form amphibole. In pyroxenites, most of the clinopyroxene is transformed into amphibole.

A particular feature of the mylonites and ultramylonites is their exceptionally high proportion of amphibole (up to 30 vol%) with respect to the rest of the northern shear zone. Three different types of amphibole have

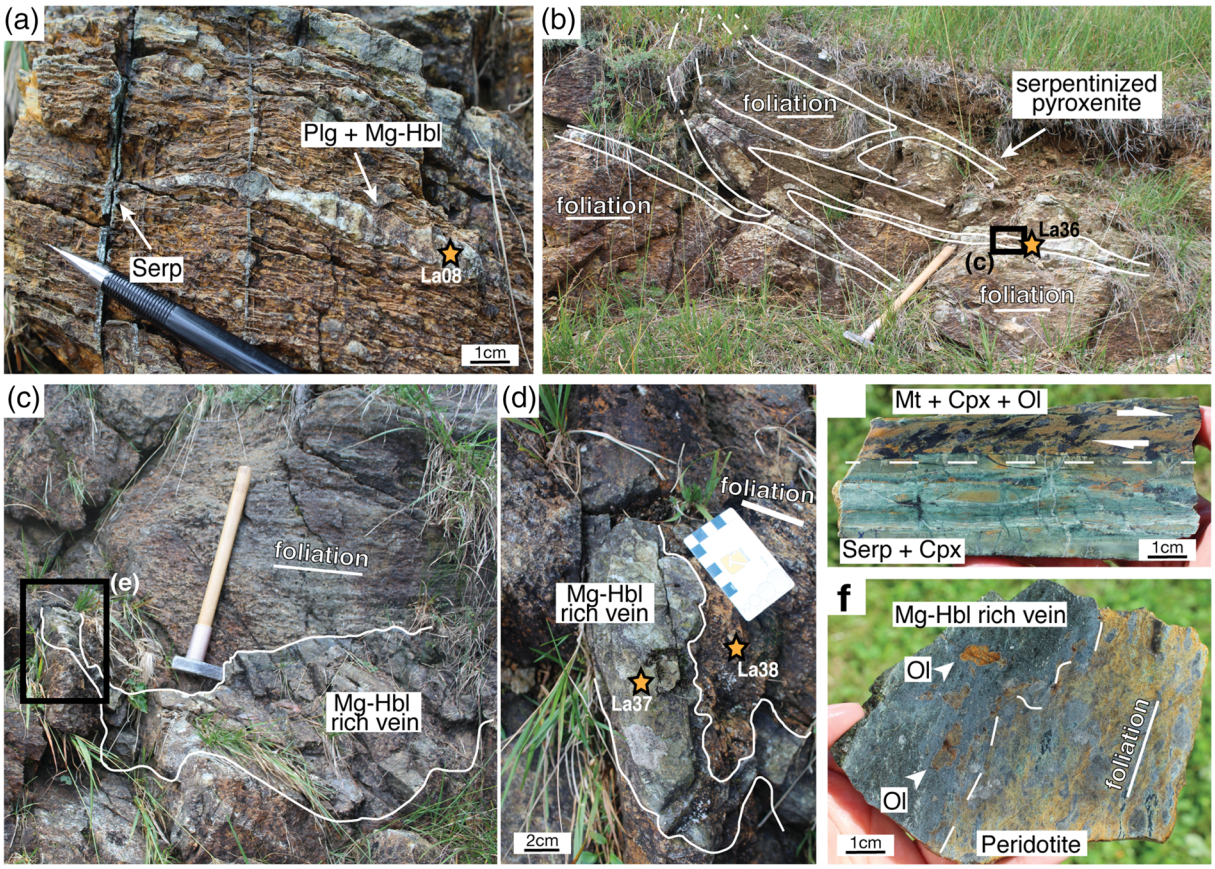

Figure 3. Images showing evidence for melt and fluid percolation. (a) Gabbroic dikelet stretching parallel to the high-temperature foliation and forming cm-scale boudins of plagioclase and Mg-hornblende. (b, c) Anastomosing dikelets of mylonitized and serpentinized pyroxenite showing dextral sense of shear. (d–f) Intensely deformed Mg-hornblende-rich vein. Sampling sites are indicated by yellow stars, and sample description is available in Table 1. Ol = olivine; Opx = orthopyroxene; Cpx = clinopyroxene; Plg = plagioclase; Am = amphibole; Serp = serpentine; Mg-Hbl = Mg-hornblende; Spl = spinel; Mt = magnetite; Chl = chlorite; Krs = kaersutite; Tr = tremolite.

been distinguished (Figure 5): (a) light brown Mg-hornblende is the most common amphibole type found in all rocks, with increasing modal abundance from the protomylonites to both the mylonites and ultramylonites. In protomylonitic gabbro dikelets, it takes the form of sheared porphyroclasts embedded in a fine-grained plagioclase and clinopyroxene matrix (Figure 5a). When associated with orthopyroxene, it replaces clinopyroxene along cleavage/exsolution planes or forms acicular crystals between sheared porphyroclasts (Figure 5b). (b) Dark brown kaersutite forms grains up to 200 μm in size embedded in the ultramylonitic matrix of the shear plane P4 (Figure 5c). (c) Light green tremolite is acicular and grows along reaction zones between the gabbro dikes and the wall rock peridotite (Figure 5d).

4.2. Mineral chemistry

4.2.1. Amphibole

Electron probe microanalyses (EPMAs) of the three types of amphibole are summarized in Table 2 and illustrated in Figure 6. Light brown hornblende has a composition defined by the end-members Mg-tarami-te, Mg-katophorite, and edenitic hornblende, collectively termed Mg-hornblende here (Mg-Hbl). Its Si and edenitic (K + Na in the A site) contents range between 6.31 and 6.70 apfu and between 0.6 and 0.9 apfu, respectively. Titanium is between 0.06 and 0.18 apfu (0.49–1.67 wt% TiO_2), Cr between 0.07 and 0.19 apfu (0.65–1.66 wt% Cr_2O_3), and the Mg# (molar Mg/(Mg + Fe_{tot})) between 0.87 and 0.92. Chlorine content of Mg-Hbl is extremely variable, ranging from 0.03 up to 0.15 apfu (0.15–0.61 wt%), where the highest values were measured in a mylonitic pyroxenite. Hornblende compositions from the Ronda massif (Précigout et al., 2017), Cabo Ortegal (Tilhac et al., 2016), and Zabargad Island (Agrinier et al., 1993) have similar compositions to Mg-hornblende from Lanzo, except with lower Ti. Hornblende from a transform

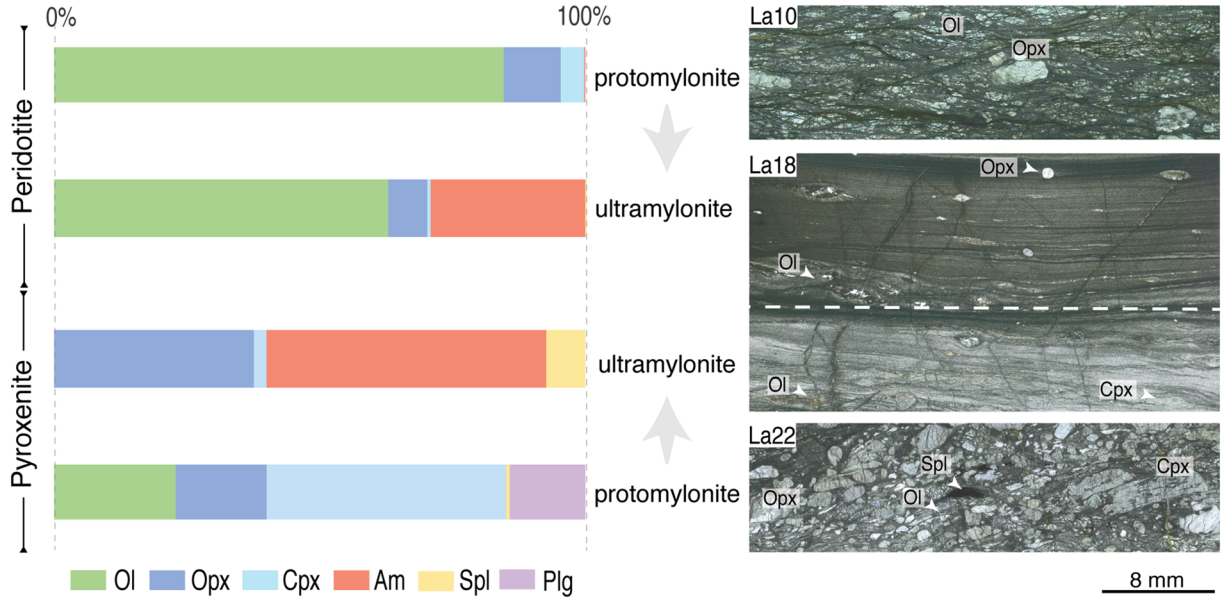

Figure 4. Mineral modal abundances inferred from EBSD phase maps. Abbreviations as in Figure 3.

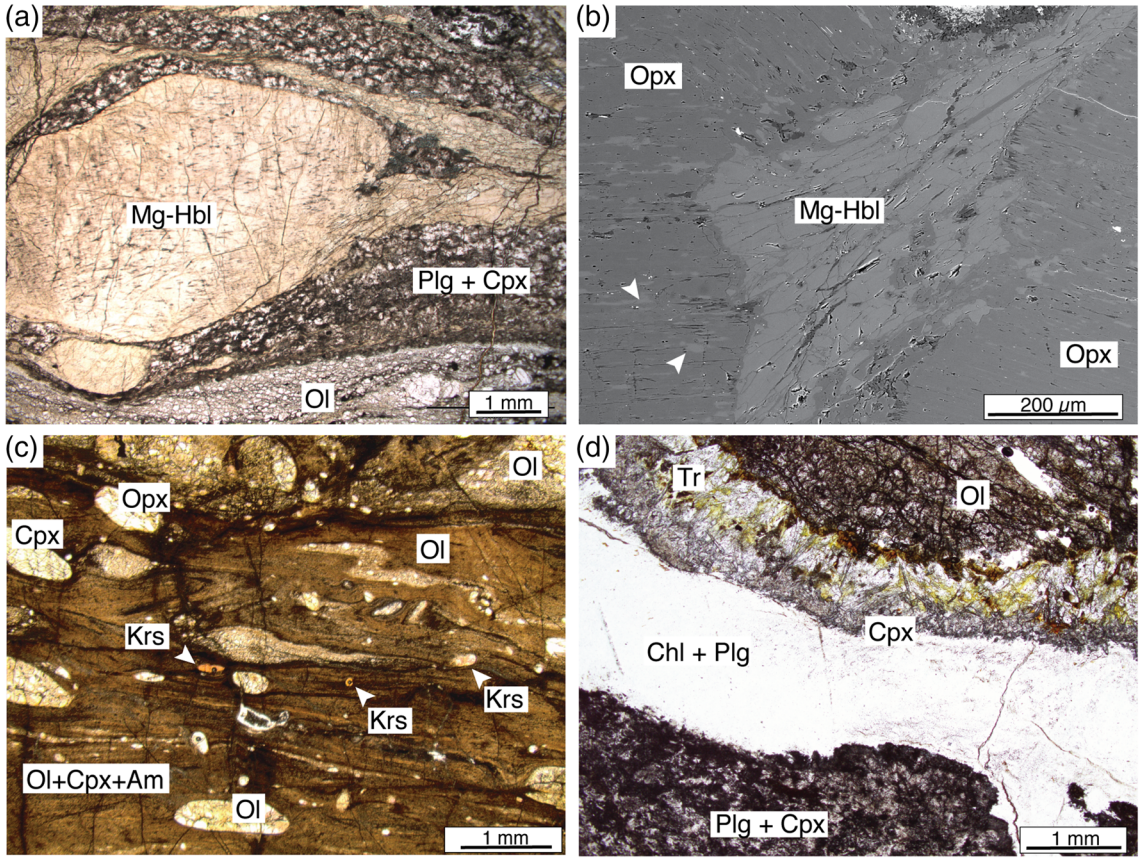

Figure 5. Photomicrographs showing the different types of amphibole observed in the hydrous mylonite zone. (a) Deformed Mg-hornblende in gabbro (Sample La08). (b) BSE image of Mg-hornblende replacing orthopyroxene (Sample La27). (c) Rounded kaersutite grains embedded in an ultramylonitic matrix of olivine, clinopyroxene, and amphibole stretching in shear plane P4 (Sample La32). (d) Late tremolite along with clinopyroxene bordering a vein of chlorite and plagioclase (Sample La08). Abbreviations as in Figure 3.

Journal of Geophysical Research: Solid Earth
10.1029/2020JB019509

Table 2
Amphibole Compositions Obtained by EPMA and Grouped by Microtexture and Lithology

	Protomylonite								Mylonite						Ultramylonite					
	Gabbro				Peridotite		Hbl vein		Peridotite		Pyroxenite				Peridotite		Pyroxenite		Peridotite	
	Mg-Hbl		Tremolite vein		Mg-Hbl		Mg-Hbl		Mg-Hbl		Mg-Hbl				Mg-Hbl		Mg-Hbl		Kaersutite	
	La06		La06		La14		La37		La04, La20		La19		La24		La18		La18		La32	
	$n = 11$	1σ	$n = 2$	1σ	$n = 5$	1σ	$n = 5$	1σ	$n = 11$	1σ	$n = 2$	1σ	$n = 4$	1σ	$n = 8$	1σ	$n = 10$	1σ	$n = 12$	1σ
wt%																				
SiO_2	46.95	0.30	58.26	0.03	45.57	0.85	46.97	1.04	46.85	0.95	46.15	0.74	44.48	0.43	46.19	1.08	46.07	0.94	43.27	0.48
TiO_2	0.95	0.18	<0.01	—	1.19	0.09	0.61	0.05	0.71	0.13	0.64	0.05	1.62	0.04	1.13	0.23	0.89	0.27	5.47	0.12
Cr_2O_3	1.14	0.18	<0.01	—	1.31	0.12	1.26	0.08	1.37	0.32	1.45	0.06	1.32	0.04	1.02	0.29	1.21	0.19	1.28	0.20
Al_2O_3	10.45	0.32	0.69	0.01	11.16	0.63	10.02	0.58	10.52	0.86	10.87	0.53	11.85	0.14	10.54	0.79	10.79	0.55	12.18	0.28
FeO	3.83	0.18	2.05	0.06	4.30	0.34	4.02	0.08	4.05	0.28	3.87	0.24	4.41	0.16	3.85	0.10	3.92	0.20	4.76	0.14
MnO	0.06	0.02	0.04	0.01	0.04	0.03	0.02	0.01	0.03	0.01	0.08	0.01	0.06	0.03	0.04	0.02	0.05	0.02	0.03	0.01
NiO	0.11	0.01	0.20	0.01	0.12	0.02	0.12	0.02	0.11	0.02	0.12	0.01	0.12	0.01	0.10	0.01	0.11	0.02	0.10	0.01
MgO	18.65	0.20	22.81	0.42	18.88	0.28	19.92	0.22	19.54	0.46	18.69	0.25	17.48	0.19	18.10	0.53	18.31	0.68	15.43	0.25
CaO	12.14	0.06	9.90	0.15	12.31	0.11	12.26	0.05	12.36	0.06	12.24	0.18	12.00	0.12	12.22	0.13	12.25	0.17	12.23	0.06
Na_2O	3.27	0.58	3.63	0.14	3.26	0.17	2.19	0.13	2.70	0.28	2.74	0.01	3.55	0.11	2.78	0.34	2.92	0.25	3.10	0.15
K_2O	0.04	0.01	0.17	0.01	0.04	0.01	0.04	0.01	0.04	0.01	0.04	0.01	0.04	0.01	0.04	0.01	0.05	0.01	1.03	0.12
Cl	0.20	0.03	0.02	0.00	0.31	0.06	0.15	0.01	0.23	0.04	0.28	0.02	0.46	0.08	0.27	0.04	0.29	0.03	0.06	0.03
Total	97.8	0.30	97.77	0.48	98.47	0.63	97.58	0.67	98.51	0.78	97.15	0.32	97.37	0.16	96.28	0.86	96.87	1.13	98.94	0.57
Atoms per formula unit (apfu)																				
Si	6.63	0.04	7.97	0.03	6.44	0.09	6.63	0.10	6.58	0.10	6.57	0.07	6.38	0.05	6.62	0.15	6.58	0.08	6.14	0.05
Ti	0.10	0.02	0.00	0.00	0.13	0.01	0.06	0.01	0.08	0.01	0.07	0.01	0.17	0.00	0.12	0.03	0.10	0.03	0.58	0.01
Cr	0.13	0.02	0.00	0.00	0.15	0.01	0.14	0.01	0.15	0.04	0.16	0.01	0.15	0.00	0.12	0.03	0.14	0.02	0.14	0.02
Al	1.74	0.05	0.11	0.00	1.86	0.11	1.67	0.10	1.74	0.15	1.82	0.10	2.00	0.03	1.78	0.13	1.82	0.11	2.04	0.04
Fe^{3+}	0.09	0.00	0.05	0.00	0.10	0.01	0.09	0.00	0.10	0.01	0.09	0.01	0.11	0.00	0.09	0.00	0.09	0.01	0.11	0.00
Fe^{2+}	0.36	0.02	0.19	0.01	0.41	0.03	0.38	0.01	0.38	0.03	0.37	0.02	0.42	0.02	0.37	0.01	0.37	0.02	0.45	0.01
Mn	0.01	0.00	0.00	0.00	0.00	0.00	0.00	0.00	0.00	0.00	0.01	0.00	0.01	0.00	0.00	0.00	0.01	0.00	0.00	0.00
Ni	0.01	0.00	0.02	0.00	0.01	0.00	0.01	0.00	0.01	0.00	0.01	0.00	0.01	0.00	0.01	0.00	0.01	0.00	0.01	0.00
Mg	3.93	0.04	4.65	0.07	3.98	0.07	4.19	0.03	4.09	0.10	3.97	0.04	3.73	0.05	3.87	0.11	3.90	0.11	3.26	0.05
Ca	1.84	0.01	1.45	0.03	1.86	0.01	1.86	0.02	1.86	0.02	1.87	0.02	1.84	0.02	1.88	0.02	1.88	0.04	1.86	0.01
Na	0.89	0.16	0.96	0.03	0.89	0.05	0.60	0.04	0.74	0.08	0.75	0.00	0.99	0.03	0.77	0.10	0.81	0.07	0.85	0.04
K	0.01	0.00	0.03	0.00	0.01	0.00	0.01	0.00	0.01	0.00	0.01	0.00	0.01	0.00	0.01	0.00	0.01	0.00	0.19	0.02
H	1.95	0.01	1.99	0.00	1.93	0.01	1.96	0.00	1.95	0.01	1.93	0.00	1.89	0.02	1.94	0.01	1.93	0.01	1.99	0.01
Cl	0.05	0.01	0.00	0.00	0.07	0.01	0.04	0.00	0.05	0.01	0.07	0.00	0.11	0.02	0.06	0.01	0.07	0.01	0.01	0.01
Total	15.74	0.09	15.44	0.05	15.83	0.06	15.65	0.06	15.73	0.05	15.70	0.02	15.82	0.04	15.65	0.11	15.71	0.05	15.65	0.03
Mg#	0.90	0.00	0.95	0.00	0.89	0.01	0.90	0.00	0.90	0.01	0.90	0.01	0.88	0.00	0.89	0.00	0.89	0.01	0.85	0.01
K + Na(A)	0.74	0.09	0.44	0.05	0.83	0.06	0.61	0.04	0.72	0.06	0.70	0.02	0.82	0.04	0.65	0.11	0.71	0.05	0.65	0.03

Note. Amphibole classification after Leake et al. (1997). Formula based on 46 charges, with a fixed $Fe^{3+}/Fe_{tot} = 0.20$; $Mg\# = Mg/(Fe_{tot} + Mg)$.

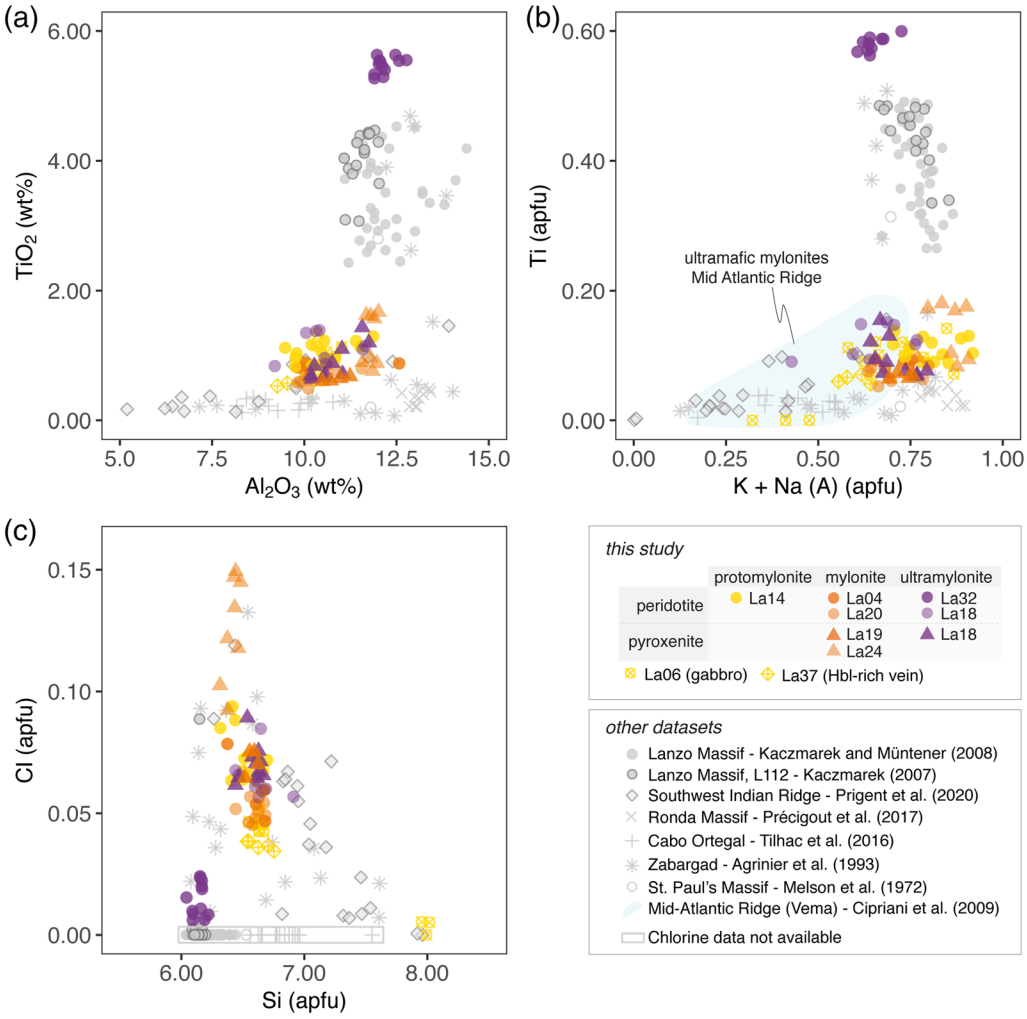

Figure 6. EPMA major element chemical data of amphibole compared with data from the literature: Ti-hornblende from the Lanzo northern shear zone (Kaczmarek, 2007; Kaczmarek & Müntener, 2008), Mg-hornblende from the Ronda massif (Hidas et al., 2016; Précigout et al., 2017) and Cabo Ortegal (Tilhac et al., 2016), Ti-hornblende, Mg-hornblende, and tremolite from Zabargad Island (Agrinier et al., 1993) and from oceanic transform faults in the Southwest Indian Ridge (Prigent et al., 2020), Mg-hornblende from the ultramafic mylonites of the Vema transect in the Mid-Atlantic Ridge (Cipriani et al., 2009), and pargasitic and kaersutitic hornblende from St. Paul's massif (Melson et al., 1972). Note that amphibole Cl concentrations are only available for Zabargad Island, Southwest Indian Ridge, and for Sample L112 in the Lanzo northern shear zone (Kaczmarek, 2007).

fault system in Southwest Indian Ridge (Prigent et al., 2020) shows, however, lower Al and lower edenite component. Amphiboles from the Southwest Indian Ridge and those from Zabargad Island display heterogeneous Cl contents, varying between 0.01 and 0.13 apfu (0.03 and 0.55 wt%).

Dark brown kaersutite (La32) is defined by high Ti contents ranging between 0.59 and 0.60 apfu. Mg# ranges between 0.872 and 0.886. Chlorine in kaersutite is lower than that of the Mg-hornblende, with values below 0.02 apfu (<0.10 wt%). Kaersutite shows similar composition to K-poor Ti-pargasite (Ti 0.27–0.43 apfu) from the Lanzo massif (Kaczmarek & Müntener, 2008) and also to Ti-pargasite from the Zabargad Island peridotites (Agrinier et al., 1993) and from St. Paul's rocks (Melson et al., 1972).

Light green tremolite has a low content of Al (0.08–0.11 apfu), while Ti and Cr are below detection limit. Mg# varies between 0.961 and 0.967. As for kaersutite, the Cl content in tremolite is very low, showing values <0.01 apfu.

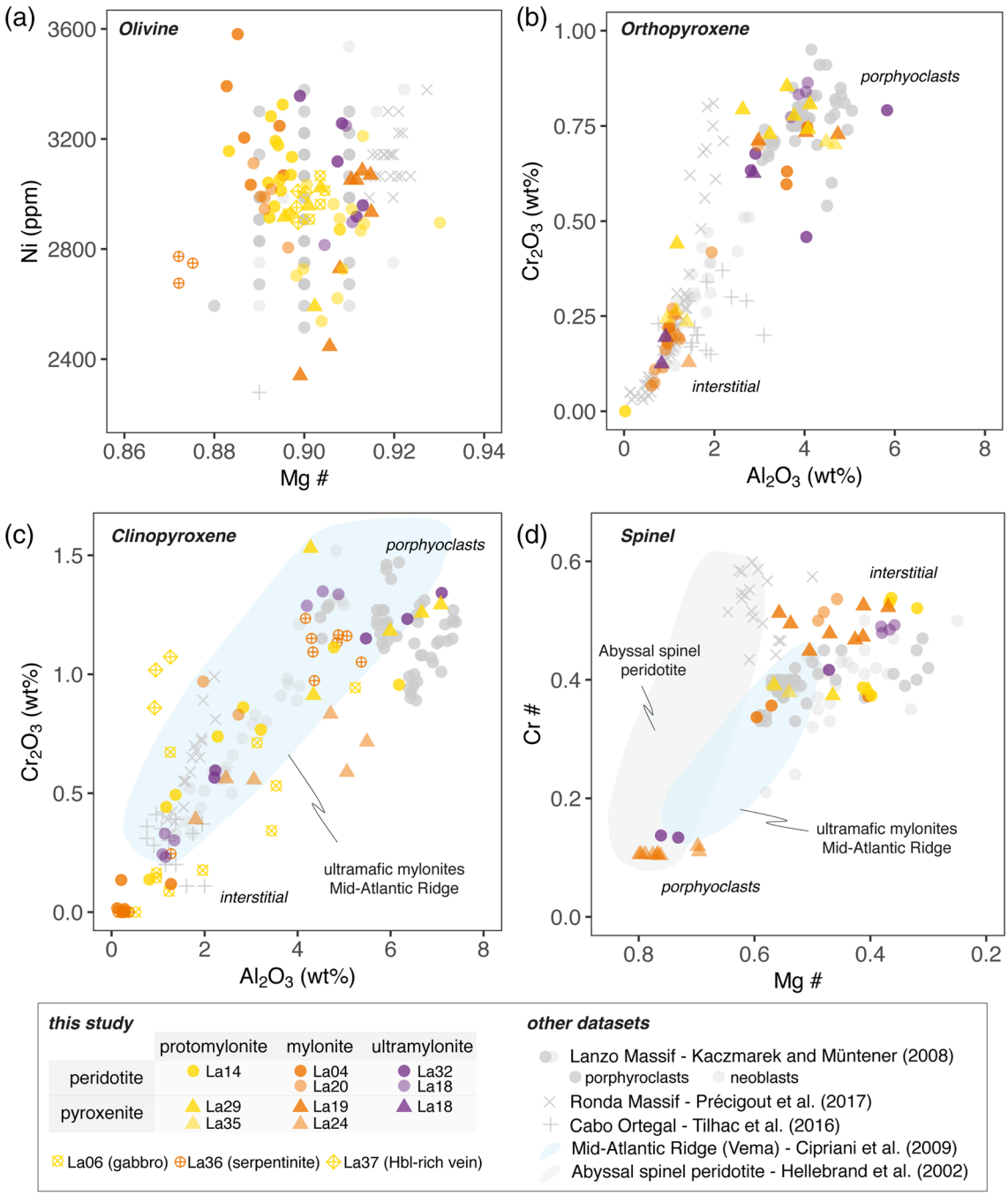

Figure 7. EPMA major element chemical data of olivine, orthopyroxene, clinopyroxene, and spinel compared with data obtained in other locations: Lanzo northern shear zone (Kaczmarek & Müntener, 2008), Ronda massif (Hidas et al., 2016; Précigout et al., 2017), and Cabo Ortegal (Tilhac et al., 2016). The abyssal spinel peridotite field (Hellebrand et al., 2002) and the ultramafic mylonite field of the Vema transform fault system in the Mid-Atlantic Ridge (Cipriani et al., 2009) are shaded in light blue.

4.2.2. Olivine

Olivine has a forsteritic composition, with Mg# that varies between 0.89 and 0.91 (Figure 7a and supporting information Data Set S1). Nickel varies between ~2,700 and 3,300 ppm, typical for mantle peridotites. A clear distinction in the olivine geochemical signature can be made between peridotite and pyroxenite rocks, with, in general, lower Mg# and higher Ni content in the former. Mg# usually decreases from protogranular to mylonitic rocks, even though olivine in ultramylonites sometimes shows Mg# similar to those observed in mylonitic pyroxenites. Matrix and recrystallized grains exhibit higher Mg# than

porphyroclasts. Olivine grains from the Mg-Hbl-rich vein and the gabbro veinlet plot within the range of olivine from the peridotite.

4.2.3. Orthopyroxene

Orthopyroxene has an enstatite-rich composition, with Mg# ranging between 0.89 and 0.92 (Data Set S2). The Al_2O_3 content varies from 0.02 to 5.83 wt%, along with an increase of the Cr_2O_3 content from 0.07 to 0.85 wt% and CaO from 0.10 to 1.50 wt% (Figure 7b). The composition of the matrix grains is more homogeneous than that of the porphyroclasts but with lower Cr, Al, and Ca contents. Orthopyroxene porphyroclasts and neoblasts from Cabo Ortegal all plot in the field of matrix grains ($Cr_2O_3 < 0.37$ wt%), even though they have slightly higher Al_2O_3 contents. The composition of Ronda orthopyroxene is generally similar to the Lanzo orthopyroxene.

4.2.4. Clinopyroxene

Clinopyroxene is close to diopside with Mg# ranging between 0.89 and 0.96 (Data Set S3). Aluminum and chromium are positively correlated, with Al_2O_3 contents ranging from 0.12 to 8 wt% and Cr_2O_3 from below detection to 1.53 wt% (Figure 7c). In the hydrous mylonite zone, Al_2O_3, Cr_2O_3, and TiO_2 values are usually lower in matrix and acicular clinopyroxene than in porphyroclasts and exsolution lamellae, except for Ti, which is sometimes higher in the former than in the latter. Aluminum and titanium are positively correlated, indicating that Ti is controlled by the Ti-Tschermak substitution. Porphyroclasts, exsolution lamellae within orthopyroxene, and matrix clinopyroxene associated with amphibole are similar to clinopyroxene porphyroclasts from the entire shear zone (e.g., Kaczmarek & Müntener, 2008), containing more than 4 wt% Al_2O_3 and more than 0.8 wt% Cr_2O_3, with a few exceptions in Sample La14 (protomylonite peridotite near shear plane P1, Figure 2). In contrast, clinopyroxene grains from Cabo Ortegal and Ronda samples display lower Al and Cr similar to matrix clinopyroxene observed in Lanzo.

4.2.5. Spinel

Spinel compositions plot in two clusters corresponding to porphyroclasts and matrix grains. However, no systematic correlation is observed between spinel composition and the degree of deformation (Figure 7d and Data Set S4). The porphyroclasts show the lowest Cr# (molar Cr/(Cr + Al)) between 0.10 and 0.14 and the highest Mg# between 0.70 and 0.80, and Fe^{3+} is generally <0.07 apfu. Mg# varies between 0.32 and 0.80 for porphyroclasts and between 0.05 and 0.11 for neoblasts and porphyroclast rims. The TiO_2 contents range from 0.04 to 0.58 wt% in porphyroclasts or up to 0.94 wt% in matrix grains. All matrix spinel analyses plot outside the abyssal spinel peridotite field (Hellebrand et al., 2002) and are shifted to higher Mg# values. Lanzo samples partially overlap the field of Mid-Atlantic Ridge peridotites (Cipriani et al., 2009).

4.3. Oxygen Isotope Data

The whole-rock $\delta^{18}O$ values from Lanzo, together with those from Zabargad Island (Agrinier et al., 1993) and from multiple ocean drilling programs (ODPs) along with global mid-ocean ridges, are plotted in Figure 8. Lanzo whole-rock $\delta^{18}O$ signatures range between 4.2‰ and 5.6‰ (Table 3). The upper bound was obtained in the ultramylonitic shear plane P4 and is very close to the mantle value of ~5.7‰ (Muehlenbachs, 1987). The lower bound was measured in the anastomosed and discordant serpentinized pyroxenite, located to the north of the studied transect. The samples in between do not show a clear correlation between $\delta^{18}O$ and texture, whether they be protogranular, protomylonitic, or mylonitic. Mineral separate $\delta^{18}O$ value of 5.5‰ has been obtained from amphibole grains separated from a folded hornblende-rich vein located in the north of the studied transect.

The relatively narrow range of isotopic compositions in the hydrous mylonite zone overlaps with the whole-rock $\delta^{18}O$ signature of the Zabargad Island peridotite (Agrinier et al., 1993). All those values are within the wide spectrum of $\delta^{18}O$ signatures observed in serpentinites from different localities of mid-ocean ridges, and in oceanic gabbros, for which values ranging between 1.9‰ and 11.2‰ (Mével, 2003), and between 3.9‰ and 8.1‰ (Talbi & Gauthier-Lafaye, 1999), are reported, respectively. Amphibole isotopic signatures display also considerable variation. In gabbro and amphibolite drill cores from the Hess Deep and from the Romanche and Vema fracture zones, $\delta^{18}O$ values range between 2.8‰ and 5.1‰ (Früh-Green et al., 1996; Talbi & Gauthier-Lafaye, 1999), whereas in the mylonitic peridotite from MOR-Vema (Cipriani et al., 2009), $\delta^{18}O$ values are between 5.5‰ and 8.8‰. The single amphibole value from the hydrous mylonite zone plots between both signatures.

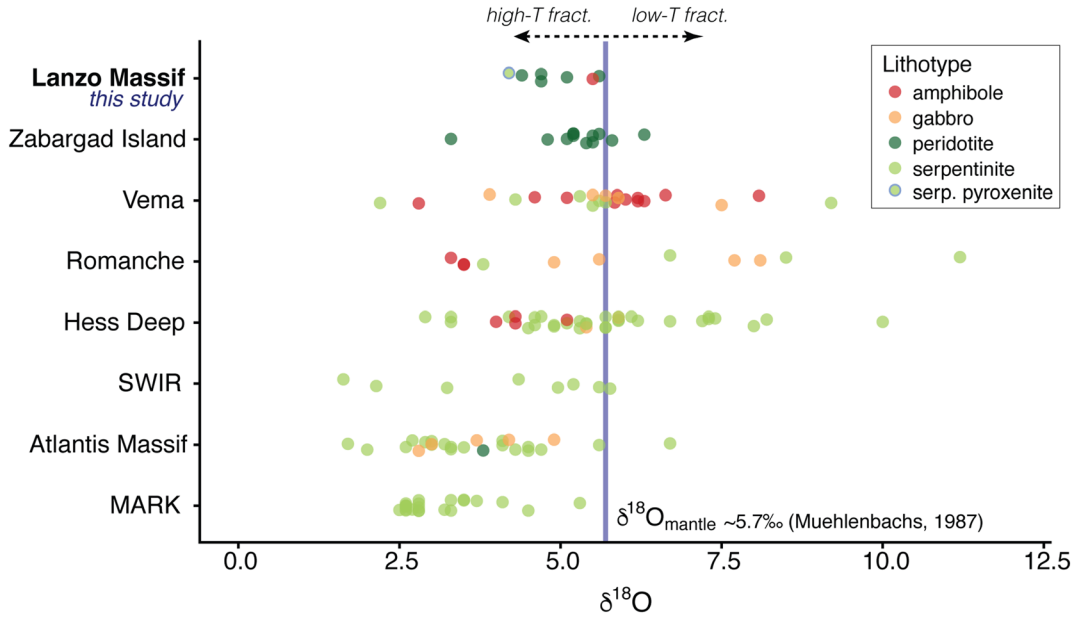

Figure 8. Oxygen isotopic signatures ($\delta^{18}O$) for amphibole and whole-rock samples of peridotite, serpentinite, and gabbro from different localities in mid-ocean ridges and ophiolites. The blue line represents the mantle/MORB reference value of ~5.7‰ (Muehlenbachs, 1987). The Lanzo $\delta^{18}O$ data are those measured in this study. Errors are within the size of the symbols. Data from other locations are shown for comparison: Romanche and Vema (Bonatti et al., 1984; Cipriani et al., 2009; Talbi & Gauthier-Lafaye, 1999), Hess Deep (Agrinier et al., 1995; Früh-Green et al., 1996), Zabargad Island (Agrinier et al., 1993), SWIR (Decitre et al., 2002), Atlantis Massif (Boschi et al., 2008), and MARK (Agrinier & Cannat, 1997).

4.4. Mineral Deformation and Fabrics

Different olivine fabrics have been observed in the protogranular, protomylonitic, and mylonitic samples on one side and in the ultramylonitic samples on the other side (Figures 9 and S3). Those two fabrics refer to the A and E types of Jung and Karato (2001), respectively. In the former, olivine shows CPO characterized by distinct [100] maxima at low angles (<10°) to the lineation (*X*), one group with [010] axes normal to the foliation (*Z*, e.g., Figure 9a) and another one with [010] axes normal to the lineation within the foliation plane (*Y*, e.g., Figure 9b). The fabric strength is low, with J-index and M-index varying between 1.40 and 2.74 and between 0.04 and 0.13, respectively (Figures 9a and 9b). In the mylonitic samples the fabric is weaker (J-index between 1.36 and 1.69), but they show similar patterns (Figure S3). Olivine porphyroclasts display strong intracrystalline deformation, with low-angle boundaries (LABs) oblique to the *X* and *Z* directions and perpendicular to the plane defined by recrystallized olivine grains (Figure 9b). In the protogranular

Table 3
Oxygen Isotope Data ($\delta^{18}O$, in ‰) of Six Whole-Rock (WR) Samples and One Amphibole Separate, Together With Mineral Modal Abundances and Rock Microtextures

Sample	Lithology/separate type	Modal proportions (vol%)								Microtexture	$\delta^{18}O$ (‰)
		Ol	Opx	Cpx	Spl	Plg	Am	Serp	Mt		
La37	Amphibole						100			Protogranular	5.5
La38 (WR)	Harzburgite	55	35	1	3	4	2			Protogranular	4.4
La14 (WR)	Lherzolite	40	30	13	4	5	8			Protomylonite	4.7
La04 (WR)	Lherzolite	55	12	10	3	5	15			Mylonite	4.7
La20 (WR)	Lherzolite	35	15	7	3	10	30			Mylonite	5.1
La36 (WR)	Pyroxenite serpentinized	7		9				76	8	Mylonite	4.2
La34 (WR)	Lherzolite	42	15	30	3		10[a]			Ultramylonite	5.6

Note. Abbreviations as in Figure 3.
[a]Including kaersutite and Mg-hornblende.

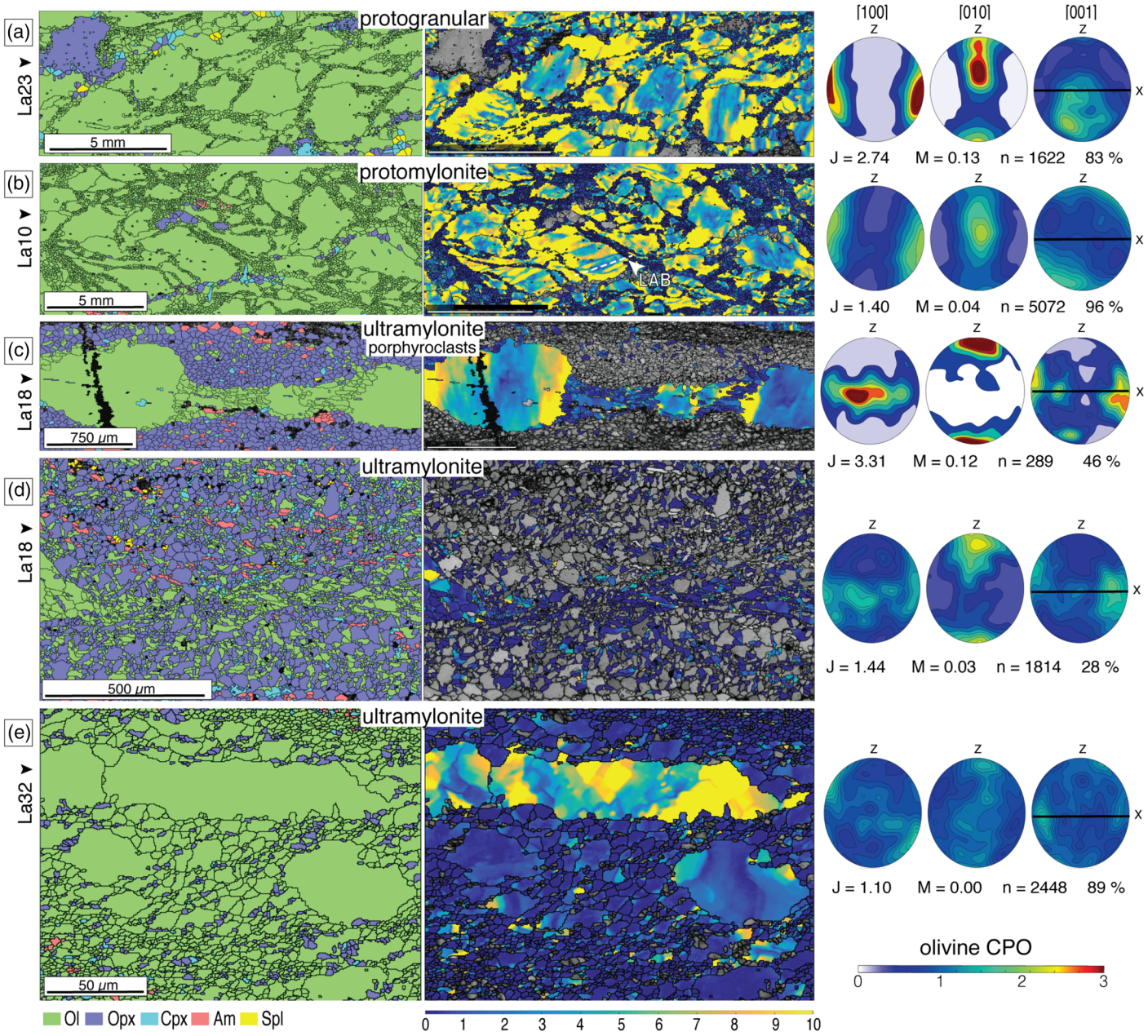

Figure 9. EBSD data for olivine in protogranular, protomylonite, and ultramylonites of the hydrous mylonite zone, displayed as phase maps (left), misorientation maps (middle), and pole figures (right). (a) Protogranular peridotite. (b) Protomylonite peridotite. (c) Olivine porphyroclasts in ultramylonitic pyroxenites. (d) Olivine grains adjacent to the olivine porphyroclasts in the ultramylonitic pyroxenite matrix. (e) Ultramylonite peridotite. Abbreviations as in Figure 3. In misorientation maps, deviation is indicated with respect to the reference orientation (average orientation of the grain: dark blue = 0°). Pole figures are lower-hemisphere equal-area projections with contours expressing multiples of uniform distribution. Fabric strength is indicated by J-index and M-index, the number of grains by *n*, and the modal abundance of olivine by vol%.

and the protomylonite the rotation axes accommodating LABs (2–15°) within olivine grains have a rotation on <0vw>, which is better develop either around [001] or [010] varying from sample to sample (Figure S3). The detailed study of the olivine porphyroclasts from a pyroxene-rich ultramylonitic matrix (Sample La18) shows pole figures with a strong point concentration of [010] axes parallel to *Z* and weak [001] and [100] maxima parallel to *X* and *Y*, respectively (Figure 9c). With J-index and M-index of 3.31 and 0.12, the fabric of olivine porphyroclasts is stronger in the pyroxene-rich ultramylonite than those of the protogranular and protomylonite peridotites. Intracrystalline deformation is indicated by LABs parallel to *Z* in the cores but

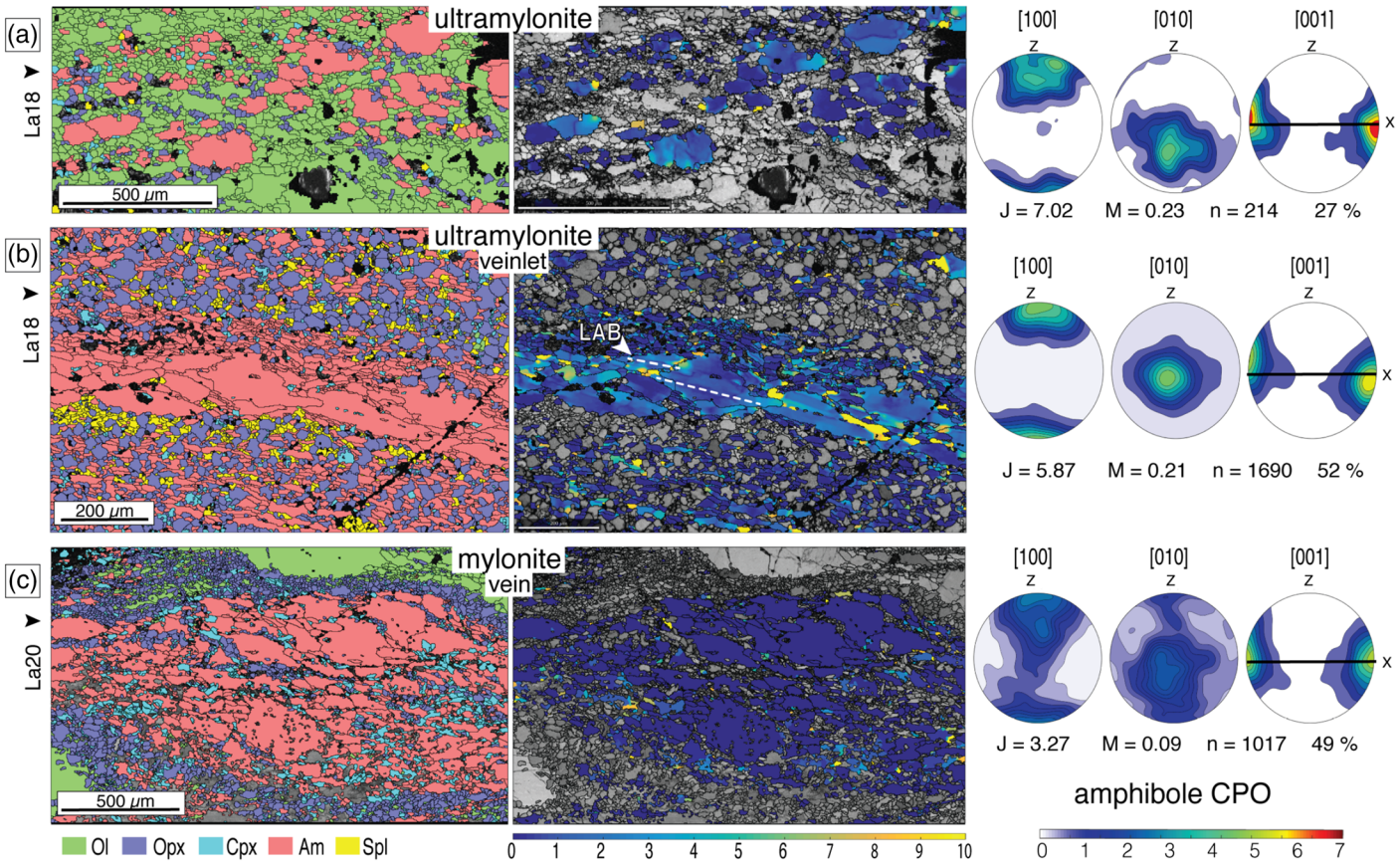

Figure 10. EBSD data for amphibole in mylonites and ultramylonites of the hydrous mylonite zone, displayed as phase maps (left), misorientation maps (middle), and pole figures (right). (a) Peridotite ultramylonitic matrix. (b) Veinlet in ultramylonitic pyroxenites showing elongated grain shapes and low-angle boundaries (LABs) parallel to the lineation (*X*). (c) Boudinaged vein in mylonitic gabbroic peridotites. Abbreviations as in Figure 3. Legends for maps and pole figures as in Figure 9.

with deviations up to 10° (or more) at the grain tips. The olivine porphyroclast is embedded in a pyroxene-rich matrix, which is well illustrated in Figure 9d. In the ultramylonitic pyroxenite and peridotite the neoblasts show less intracrystalline deformation than the nearby porphyroclasts and only a weak shape preferred orientation (Figures 9d and 9e). [010] axes form a distinct maximum parallel to *Z*, while [100] axes form a girdle within the foliation plane, and [001] axes form a weak concentration point (or girdle) parallel to *X* (Figures 9d, 9e, and S3). The fabric is slightly weaker than that of the porphyroclasts, with J-index varying from 1.10 to 1.44 and M-index <0.03.

Amphibole grains disseminated in the ultramylonite matrix are elongated and show obvious shape preferred orientation (Figure 10), with grain sizes ranging between 25 and 250 μm. Most of them display only weak internal deformation mainly associated with grain boundaries (Figure 10a). When clustered into veinlets, amphibole forms even more elongated grains showing LABs subparallel to *X* (Figure 10b). In centimetric gabbroic veins (Samples La06, La08, and La20), the amphibole grains vary from large porphyroclasts showing important internal deformation to recrystallized grains with weak internal deformation (Figure 10c). In the vein from a mylonitic sample, amphibole grains up to 500 μm are observed (Figure 9c). Most of the grains have less intracrystalline deformation and show at least some subgrain boundaries. The fabric is strong and become stronger from the mylonitic gabbroic veins (J-index 2.41–5.0; M-index 0.08–0.18), to ultramylonitic peridotite (J-index: 7.02; M-index: 0.23), and pyroxenites (J-index: 4.36–10.9; M-index: 0.14–0.38; Figure S3). In all samples, amphibole [100], [010], and [001] axes point close to *Z*, *Y*, and *X*, respectively (e.g., Figure 10). In a few gabbroic veins amphibole [100] axes show an obvious dispersion in the *YZ* plane.

In addition, pyroxene fabrics (Figures 11 and S3) are weak to moderate, with only limited correlation with olivine fabric (pyroxene [001] parallel to olivine [100]). Orthopyroxene in protogranular sample show

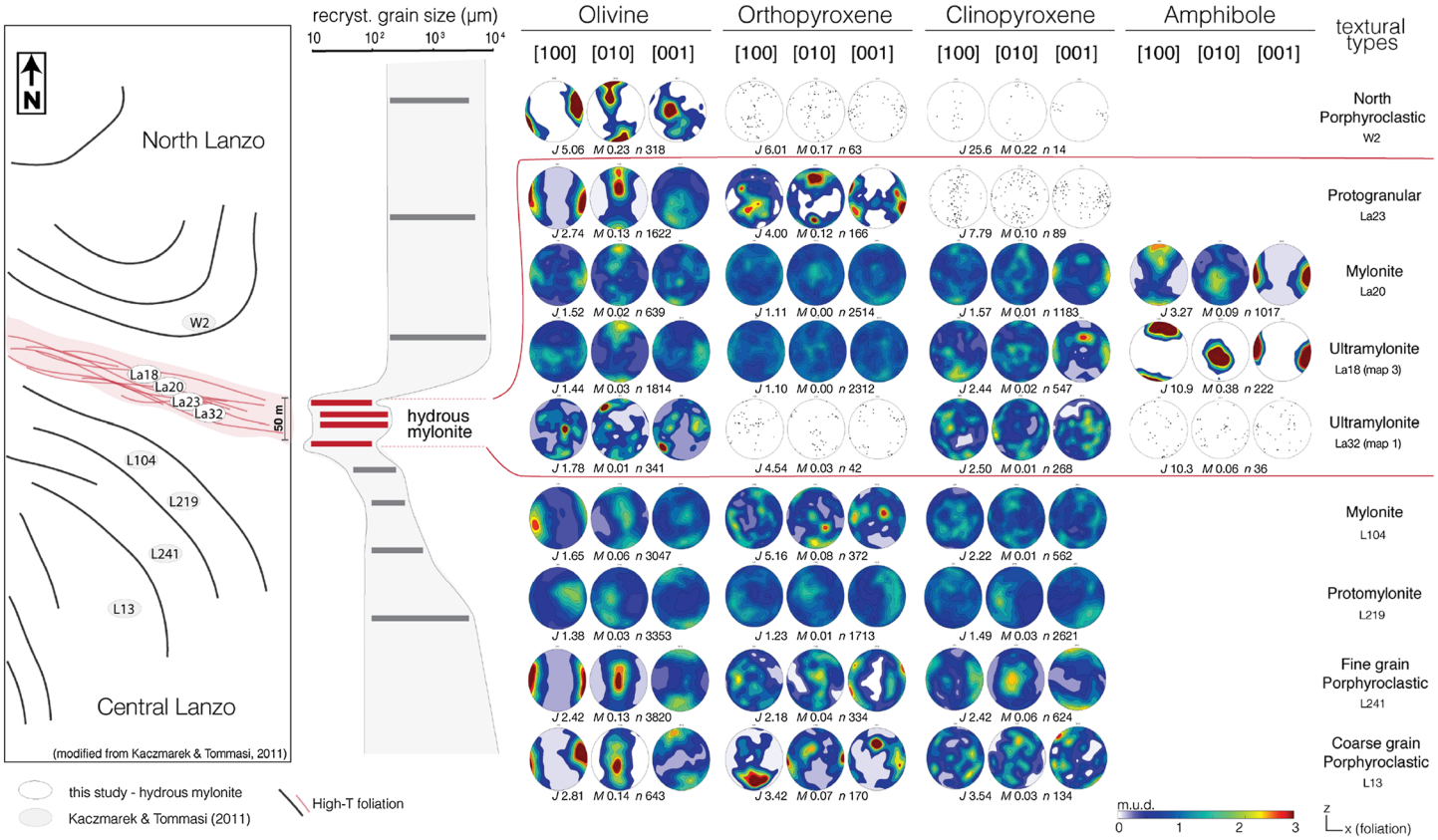

Figure 11. Summary sketch showing the correlation between the amount of seawater, the size of recrystallized grains in the peridotites, and the mineral fabrics for olivine, orthopyroxene, clinopyroxene, and amphibole. In the map, the red field indicates where Mg-hornblende is concentrated. Data outside the hydrous mylonite zone are from Kaczmarek and Tommasi (2011). Fabric strength indicators in the form of J-index and M-index are available in Data Set S5.

[010] axes parallel to *Z* and [001] axes subparallel to *X*, a fabric typical for deformation at high temperature (Jung et al., 2010; Turner et al., 1960). In protomylonite samples, the fabric is weaker, with [001] axes subparallel to *X* and [100] subparallel to *Z* (Figure S3). Mylonitic and ultramylonitic orthopyroxene fabrics are even weaker, with [100], [010], and [001] axes forming diffuse maxima parallel to *X*, *Y*, and *Z*, respectively. Even though orthopyroxene is a predominant phase in the pyroxene-rich zone of the ultramylonites, grains do not exceed 100 μm in size. Intracrystalline deformation is weaker and aspect ratios closer to unity than for olivine and amphibole, and only local misorientations related to subgrain boundaries can be detected (Figure S2). Clinopyroxene fabrics in protomylonites and mylonites display [001] and [100] axes subparallel to *X* and *Z*, respectively, while there is no clear correspondence between fabrics and structural directions in the ultramylonites. The J-index and the M-index are low, with values of 1.57 and 0.01 in the mylonites and 2.44 and 0.02 in the ultramylonites (Figure 11).

5. Discussion

The Lanzo hydrous mylonite zone records a complex history involving localized deformation and fluid circulation beyond the stability field of serpentine. We evaluate here the role of ductile deformation on the progressive hydration of the peridotite mylonites, and we discuss the origin of fluid circulation within mantle shear zones based on the Cl signature of amphibole. These arguments are combined with geophysical data from (ultraslow) slow spreading ridges to propose a geological model in which fluids reach depths beyond the serpentine stability field, that is, in the "semibrittle" regime, at temperatures higher than ~600°C and pressures lower than ~0.5 GPa.

5.1. Deformation History Recorded by Mineral Fabrics

The deformation history of the Lanzo peridotites can be reconstructed from the mineral fabrics observed in the northern shear zone and in the hydrous mylonite zone in particular. In the protogranular, porphyroclastic, protomylonitic, and some mylonitic samples, olivine is characterized by the classic A-type and the less common E-type fabrics, which result from the activation of the (010)[100] and (001)[100] slip systems, respectively (Jung & Karato, 2001; Katayama et al., 2004). Both fabrics are typical for peridotites deformed under high-temperature and low stress conditions, the main difference being the contribution of water to deformation, minimal in the A-type and moderate to low in the E-type fabric (Karato et al., 2008; Palasse et al., 2012). The olivine fabric in ultramylonitic peridotites is weak and resembles an A type. Olivine grains are not strongly elongated, suggesting an important contribution of diffusion creep. In one pyroxenite sample (La18) olivine porphyroclasts and olivine from the adjacent matrix show a [001] glide direction, which is known to be activated with high water content (Jung & Karato, 2001) (Figures 9c and 9d). This sample contains a high proportion of orthopyroxene. In a recent study on websterite, the olivine CPO suggests a glide on the [001] axes at high temperature (Hidas et al., 2013) similar to our observations. In our sample, the [001] glide direction within the (010) plane in olivine porphyroclast and in the matrix is well in line with high-temperature deformation conditions (Jung & Karato, 2001; Karato et al., 2008).

The transition to lower-temperature deformation conditions is supported by the occurrence of plastically deformed Mg-hornblende in the mylonitic and ultramylonitic mineral assemblage from all lithologies. Studies on equilibrium assemblages from ultramafic rocks during progressive metamorphism indicate that Mg-hornblende is stable with olivine, orthopyroxene, and spinel/plagioclase below ~950°C (Evans, 1982; Fumagalli et al., 2009; Niida & Green, 1999). The presence of intracrystalline deformation features, such as undulatory extinction and subgrain boundary walls in Mg-hornblende, therefore indicates that significant dislocation creep occurred in the lithosphere. This statement is further supported by the fabric type observed in Mg-hornblende, with [001] pointing to the lineation and [100] normal to the foliation, which has been reported for deformation under dislocation creep (Biermann & Van Roermund, 1983; Dollinger & Blacic, 1975; Rooney et al., 1975) at temperatures ranging between 650°C and 970°C (Berger & Stünitz, 1996; Cao et al., 2010; Díaz Aspiroz et al., 2007). This interval fits well with the equilibration temperature of 860°C obtained by Kaczmarek and Müntener (2008) from the neoblasts of the ultramylonites. The exceptionally high fabric strength and the large aspect ratios of Mg-hornblende grains are interpreted as a result of synkinematic oriented grain growth (Henry et al., 2017), followed by easy glide onto the (100)[001] slip system. This interpretation is consistent with the observations of Liu (1999) and Cao et al. (2010) that the initial orientation of amphibole grains plays a determinant role in the preferential activation of the (100)[001] slip system. Finally yet importantly, the observations that growth and deformation of Mg-hornblende were, at least in part, coeval, have the additional consequence that fluid circulation and deformation are most likely contemporaneous, in the stability field of Mg-hornblende.

Ongoing deformation is characterized by further reduction in grain size and progressive weakening of the mineral fabrics (see Figure S3) in the ultramylonitic zones. Both processes are generally attributed to dynamic recrystallization under decreasing temperature, followed by a change in deformation regime from dislocation to diffusion creep and grain boundary sliding (Evans et al., 2001). This effect is particularly significant in polymineralic assemblages, where secondary phases inhibit grain growth and contribute to the sustainability of diffusion creep over time (e.g., Linckens et al., 2011; Précigout & Gueydan, 2009; Sundberg & Cooper, 2008). These observations suggest a final deformation stage occurring at lower temperatures and shallower depths, possibly related to the exhumation of the Lanzo upper mantle. Absolute temperature estimates for this final stage are, however, difficult to distinguish from those reached during Alpine metamorphism (e.g., Pelletier & Müntener, 2006).

In summary, the mineral fabrics observed in the Lanzo hydrous mylonite zone are prime examples of progressive localization of deformation and point to the key role played by synkinematic growth of hornblende and fluid circulation in upper mantle shear zones. This suggests that strain focusing and hydration might be coupled processes during exhumation of mantle rocks, consistent with recent numerical thermomechanical models on ultraslow spreading ridges. A good example is the flat seafloor morphology of the ultraslow

spreading Southwest Indian Ridge, which can only be modeled satisfactorily by shallow level serpentinization coupled to strain focusing in the deeper mantle lithosphere (Bickert et al., 2020).

5.2. Mg-Hornblende as a Tracer of Seawater Infiltration

The chemistry of Mg-hornblende and the whole-rock $\delta^{18}O$ isotopic signatures complement the deformation history of the hydrous mylonite zone and offer constraints for the conditions and origin of fluid infiltration. Mg-hornblende shows low K and Ti but elevated Cr (0.65–1.72 wt% Cr_2O_3) and Cl (0.15–0.61 wt%) concentrations. Their chemistry is consistent with the observed assemblage Ol + Opx + Cpx + Cr-Spl + Hbl ± Plg, equally described to occur in natural samples at temperatures equivalent to the transition between amphibolite to granulite facies (Evans, 1982). The high Cr content, phase relations from field data, and thermodynamic modeling further indicate that Mg-hornblende is produced from the reaction of Opx, Cpx, and H_2O at 750°C to 850°C and ~1 GPa (Ulmer & Trommsdorff, 1999). Importantly, the Cl contents in Mg-Hbl are higher than values of Ti-pargasite from upper mantle peridotites (Agrinier et al., 1988, 1996), but they are strikingly similar to hornblende in mylonitic bands from the Zabargad Island peridotite (Agrinier et al., 1993) and those found in oceanic transform faults in the SWIR (Prigent et al., 2020). Their formation was in both cases attributed to interaction with seawater-derived fluid between 750°C and 450°C; in the first during the last stage of rifting of the Red Sea (Agrinier et al., 1993); and in the second during progressive mylonite deformation at depths of 20–25 km (Prigent et al., 2020). The amphibole-bearing mylonites from the Lanzo shear zone thus seem to indicate evidence of interaction with seawater-derived fluid in a range of temperatures constrained by the amphibole chemistry, higher than that described in Zabargad Island but similar to the deep and high-temperature mylonite deformation recorded in transform faults in the SWIR.

The abundance of hornblende and absence of serpentine in the ultramylonitic zones, and the Cl enrichment in hornblende could be interpreted as infiltration of seawater at temperatures exceeding serpentine stability. These fluids most likely reacted with pyroxenes to form amphibole. Additional evidence for an oceanic origin in the Lanzo massif include (a) the presence of ophicarbonate breccias (Pelletier & Müntener, 2006; Vitale Brovarone et al., 2017); (b) metarodingite dikes within the serpentinized part of the Lanzo massif (Pognante et al., 1985); (c) metaradiolarite and metabasalts covering parts of the Lanzo peridotite (Lagabrielle & Lemoine, 1997); and (d) boron-enriched lizardite and Eu anomaly along the contact between strongly serpentinized and fresh peridotites (Debret et al., 2013).

Oxygen isotopes performed on peridotitic samples from the hydrous mylonite zone support this premise. They show a narrow range of $\delta^{18}O$ isotopic signatures from 4.4‰ to 5.6‰ (Table 3), lying within the known range of compositions of oceanic serpentinites and gabbros. These show a large dispersion in values, between 1.6‰ and 11.2‰ in serpentinites, indicating that serpentinization reactions occur over a wide range of temperatures (Mével, 2003). From these, values lower than the MORB/mantle value are commonly interpreted as related to high-temperature hydrothermal activity, exerted by a fluid derived from seawater (Gregory & Taylor, 1981).

Chlorine-bearing hydrous phases coupled with $\delta^{18}O$, specifically, are a hallmark of hydrothermal activity, probably related to downflow of seawater into the mantle. The question is, then, why Mg-hornblende displays Cl contents that are generally exceeding concentrations reported in chlorite or serpentine. Chlorine enrichment in Mg-Hbl could be accomplished by "desiccation," which in its simplest form means that a high-temperature fluid hydrating mantle rocks would preferentially loose H_2O by crystallization of hydrous phases such as hornblende, and concomitant increase of Cl and other anions in the residual fluid. Desiccation mechanisms to enrich fluids in anions up to saturation of halite have previously been proposed for the formation of amphibole in dry lower continental crust (Kullerud & Erambert, 1999; Markl & Bucher, 1998). Along the same lines, the downflow of seawater into nearly dry peridotite could be affected by a similar desiccation mechanism. Until seawater would reach areas of high temperature favorable for the formation of Mg-hornblende, the Cl/H_2O ratio has probably changed significantly. Therefore, desiccation could explain why the Cl content of Mg-hornblende is highly variable and sometimes reaches values up to 0.6 wt%. Enrichments in Mg-hornblende with high Cl contents and $\delta^{18}O_{whole\text{-}rock}$ isotopic signatures of ca. 4.4–4.7‰ can therefore represent a seawater tracer in mantle shear zones, witnessing hydration around 800–850°C, prior to serpentinization. Future studies along (ultraslow) slow spreading ridges should test whether Cl enrichment in high-temperature amphibole is as widespread as proposed here.

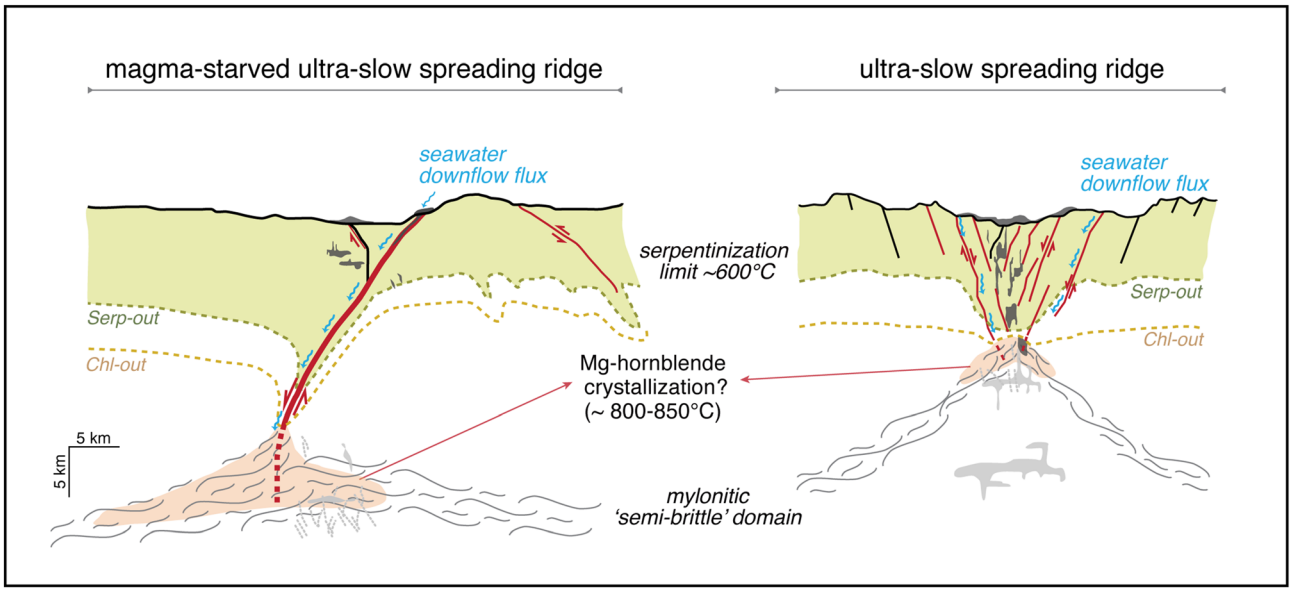

Figure 12. Conceptual illustration of the Mg-hornblende crystallization conditions at a magma-starved or magma-fed ultraslow spreading ridge setting (adapted from Cannat et al., 2019; Gillard et al., 2019). Seawater-derived fluids access the mantle lithosphere along brittle faults to temperatures above the serpentine stability, reaching a mylonitic "semibrittle" domain where synchronous growth and deformation of Mg-hornblende occurs (red-shaded area). Dark and light gray areas represent basalts and gabbros, respectively.

5.3. Implications for the Brittle-Ductile Transition in Mantle Peridotites Along Ultraslow Spreading Systems

Our findings of high-temperature hydration of mantle peridotites have far-reaching implications for the strength of the mantle lithosphere. The observations that growth and deformation of Mg-hornblende were, at least in part, coeval, imply that "brittle" fluid access and "ductile" deformation of Mg-hornblende occurred contemporaneously in the Mg-hornblende stability field. Brittle behavior enhanced by fluid influx is suggested by fractured olivine and orthopyroxene grains (e.g., Figure 5b), along which Mg-hornblende is growing and deforming ductively. Other evidence, such as compositional jumps within large orthopyroxene porphyroclasts (e.g., Figure 10 in Kaczmarek & Müntener, 2008), have also been related to brittle mineral fracturing. All those microstructures and the temperature estimates given by Mg-hornblende slip systems (Figure 10) and the thermal stability of Mg-hornblende suggest a "semibrittle" shear zone behavior beyond the stability field of serpentine at temperatures exceeding 600°C. This is schematically illustrated in Figure 12 where areas of "semibrittle" behavior in the mantle lithosphere could be identified. Certainly, the plate separation velocity has an important control on the thermal structure of ultraslow spreading ridges (e.g., Chen & Morgan, 1990), and it is difficult to predict at what depth such hornblende-rich "semibrittle" mantle shear zones would occur. For our case study in the Lanzo peridotites, hornblende formation can be constrained to about ~750–850°C, at pressures of about 0.3–0.5 GPa, which corresponds to ~9–15 km depth of the shear zone. These temperatures are higher than those estimated for the brittle failure of upper mantle beneath oceanic plates, which range between ~600 and 700 ± 50°C for a given thermal structure of the oceanic crust (Chen & Morgan, 1990; McKenzie et al., 2005). It has been argued that these temperatures might represent a "natural limit" for earthquakes in the mantle beneath oceanic plates, but these large-scale "steady-state" results are not necessarily applicable to actively deforming (ultraslow) slow spreading areas (e.g., Cannat et al., 2019). Interestingly, recent surveys along oceanic core complexes in (ultraslow) slow spreading settings along the Mid-Atlantic Ridge and Southwest Indian Ridge indicate microseismicity down to depth of 7–12 km or almost 20 km, respectively (Parnell-Turner et al., 2017; Schlindwein & Schmid, 2016; Yu et al., 2018), depending on the thermal structure of the axial lithosphere. Observations along transform faults on the East Pacific Rise have also shown that fluid-related effects may be equally important as thermal effects in controlling earthquake rupture on oceanic faults (McGuire et al., 2012). Our results indicate that Mg-hornblende formation in peridotite mylonite shear zones might represent "semibrittle" behavior, with downflow fluid, reaction weakening, and fluid-assisted strain localization in anastomosing shear zones

that reach beyond serpentine stability. Strain localization does therefore not only occur in areas of $T < 500°C$ as deduced from altered rocks sampled from the exposed footwall of detachments in oceanic core complexes (e.g., Picazo et al., 2012). Such localized high-temperature "semibrittle" shear zones might be the geological expression of the microseismicity recorded at 10–20 km depth along ultraslow spreading systems.

6. Conclusions

Magnesium-hornblende-bearing domains in mylonitic to ultramylonitic peridotites are documented in the northern part of the ophiolitic Lanzo massif, an exceptionally fresh peridotite body of the Western Tethys. Centimetric to micrometric ultramylonite and mylonite layers with variable modal composition are embedded and alternated by less deformed protomylonite peridotite, as a consequence of strain partitioning enhanced by dynamic recrystallization, mechanical mixing, and chemical processes such as mineral nucleation and growth. They form an anastomosing shear zone network. Amphibole-rich hydrous peridotite mylonite may be a fingerprint of seawater penetration beyond the stability of serpentine. CPOs of the various minerals in hydrous peridotite mylonites monitor the progressive exhumation of mantle rocks and changing environmental conditions. Olivine CPO in the protogranular, protomylonite, and some mylonite layers document, besides the A-type fabrics with activation of the (010)[100] slip system, found also across the northern shear zone, the occurrence of E-type fabrics with the activation of the (001)[100] slip system. Both are a hallmark of deformation under high-temperature and low stress conditions, characteristic in the upper mantle (Jung & Karato, 2001; Katayama et al., 2004). However, while insignificant in the A type, the E type indicates a moderate contribution of water during deformation (Karato et al., 2008). Thus, the drastic loss of the mineral CPO (e.g., olivine and pyroxenes) observed in the fine-grained matrix is a consequence of the reduction of the recrystallized grain size combined with fluid infiltration along specific structural weak zones (Holtzman et al., 2003; Katayama et al., 2004). The weaker patterns of olivine and pyroxene CPO are obtained for samples enriched in Mg-hornblende, which comports a significant amount of Cl (0.15–0.61 wt%). The strong fabric of amphibole CPO, high aspect ratio, and activation of the (100)[001] slip system all point for synkinematic Cl-rich amphibole formation at temperatures above 800°C (Cao et al., 2010; Díaz Aspiroz et al., 2007). These conditions are consistent with the elevated edenite component of Mg-hornblende, indicating stability conditions for the paragenesis Ol + Opx + Cpx + Cr-Spl + Hbl ± Plg between 750°C and 850°C (Evans, 1982; Fumagalli et al., 2009; Niida & Green, 1999; Ulmer & Trommsdorff, 1999). Moreover, Cl enrichments in high-temperature amphibole, together with a high-temperature oxygen isotope signature ($\delta^{18}O_{whole\text{-}rock}$ between 4.4‰ and 4.7‰), strongly indicate infiltration of a seawater-derived fluid at temperatures above the serpentine stability (Janecky & Seyfried, 1986), similar to what is reported in the Zabargad Island peridotite (Agrinier et al., 1993).

Finally, Cl-rich Mg-hornblende in hydrous peridotite mylonite might be the consequence of "semibrittle" fracturing and hydration, perhaps expressed as microseismicity beneath ultraslow spreading systems, and may represent a stage of strain localization and mantle hydration prior to serpentinization. These high-temperature hydrous phases formed most probably by interaction of peridotites with seawater-derived fluids, which gets enriched in Cl by reacting along pathways to greater depth, in a desiccation-like mechanism. The combined effects of grain size reduction and fluid infiltration probably form "semibrittle" peridotite mylonites, that might advance significantly beyond the ~3–6 km thick serpentinization front interpreted from seismic data. They could act as nuclei for the formation of large-scale detachment faults that are common along slow and ultraslow spreading ridges.

Data Availability Statement

Full data are available from the Zenodo repository (https://doi.org/10.5281/zenodo.3628599).

Acknowledgments

This study was supported by an Ambizione fellowship of the Swiss National Science Foundation (Schweizerischer Nationalfonds zur Förderung der wissenschaftlichen Forschung) (Grant 200020-142454) to M-A. K. Our thanks go to Martin Robyr for setting up the electron microprobe at the University of Lausanne and to Hadrien Henry and Luiz G. Morales for helping with the MTEX script. J. F. V. D acknowledges support of the Swiss National Science Foundation (Grant 200021-172688 to Thomas Pettke) during final preparation of the manuscript. Constructive reviews by Cécile Prigent and two anonymous reviewers are gratefully acknowledged.

References

Agrinier, P., & Cannat, M. (1997). Oxygen-isotope constraints on serpentinization processes in ultramafic rocks from the Mid-Atlantic Ridge (23°N). *Proceeding of the Ocean Drilling Program, Scientific Results*, *153*(20), 381–388.

Agrinier, P., Cornen, G., & Beslier, M.-O. (1996). Mineralogical and oxygen isotopic features of serpentinized recovered from the ocean/continent transition in the Iberia Abyssal Plain. *Proceeding of the Ocean Drilling Program, Scientific Results*, *149*, 541–552.

Agrinier, P., Hékinian, R., Bideau, D., & Javoy, M. (1995). O and H stable isotope compositions of oceanic crust and upper mantle rocks exposed in the Hess Deep near the Galapagos Triple Junction. *Earth and Planetary Science Letters*, *136*(95), 183–196.

Agrinier, P., Mével, C., Bosch, D., & Javoy, M. (1993). Metasomatic hydrous fluids in amphibole peridotites from Zabargad Island (Red Sea). *Earth and Planetary Science Letters*, *120*, 187–205.

Agrinier, P., Mével, C., & Girardeau, J. (1988). Hydrothermal alteration of the peridotites cored at the ocean/continent boundary of the Iberian Margin: Petrologic and stable isotope evidence. *Proceeding of the Ocean Drilling Program, Scientific Results*, *103*, 225–234.

Albers, E., Schroeder, T., & Bach, W. (2019). Melt impregnation of mantle peridotite facilitates high-temperature hydration and mechanical weakening: Implications for oceanic detachment faults. *Geochemistry, Geophysics, Geosystems*, *20*, 84–108. https://doi.org/10.1029/2018GC007783

Bachmann, F., Hielscher, R., & Schaeben, H. (2010). Texture analysis with MTEX—Free and open source software toolbox. *Solid State Phenomena*, *160*, 63–68. https://doi.org/10.4028/www.scientific.net/SSP.160.63

Bai, Q., Mackwell, S. J., & Kohlstedt, D. L. (1991). High-temperature creep of olivine single crystals 1. Mechanical results for buffered samples. *Journal of Geophysical Research*, *96*(B2), 2441. https://doi.org/10.1029/90JB01723

Bayrakci, G., Minshull, T. A., Sawyer, D. S., Reston, T. J., Klaeschen, D., Papenberg, C., et al. (2016). Fault-controlled hydration of the upper mantle during continental rifting. *Nature Geoscience*, *9*(5), 384–388. https://doi.org/10.1038/ngeo2671

Berger, A., & Stünitz, H. (1996). Deformation mechanisms and reaction of hornblende: Examples from the Bergell tonalite (Central Alps). *Tectonophysics*, *257*(2–4), 149–174. https://doi.org/10.1016/0040-1951(95)00125-5

Bickert, M., Lavier, L., & Cannat, M. (2020). How do detachment faults form at ultraslow mid-ocean ridges in a thick axial lithosphere? *Earth and Planetary Science Letters*, *533*, 116048. https://doi.org/10.1016/J.EPSL.2019.116048

Biermann, C., & Van Roermund, H. L. M. (1983). Defect structures in naturally deformed clinoamphiboles—A TEM study. *Tectonophysics*, *95*(3–4), 267–278. https://doi.org/10.1016/0040-1951(83)90072-0

Boillot, G., Féraud, G., Recq, M., & Girardeau, J. (1989). Undercrusting by serpentinite beneath rifted margins. *Nature*, *341*(6242), 523–525. https://doi.org/10.1038/341523a0

Bonatti, E. (1968). Ultramafic rocks from the Mid-Atlantic Ridge. *Nature*, *219*(5152), 363–364. https://doi.org/10.1038/219363a0

Bonatti, E. (1990). Subcontinental mantle exposed in the Atlantic Ocean on St Peter–Paul islets. *Nature*, *345*(6278), 800–802. https://doi.org/10.1038/345800a0

Bonatti, E., Colantoni, P., Della Vedova, B., & Taviani, M. (1984). Geology of the Red Sea transitional region (22°N–25°N). *Oceanologica Acta*, *7*(4), 385–398.

Boschi, C., Dini, A., Fru, G. L., & Kelley, D. S. (2008). Isotopic and element exchange during serpentinization and metasomatism at the Atlantis Massif (MAR 30°N): Insights from B and Sr isotope data. *Geochimica et Cosmochimica Acta*, *72*, 1801–1823. https://doi.org/10.1016/j.gca.2008.01.013

Boudier, F. (1978). Structure and petrology of the Lanzo peridotite massif (Piedmont Alps). *Geological Society of America Bulletin*, *89*(10), 1574. https://doi.org/10.1130/0016-7606(1978)89<1574:SAPOTL>2.0.CO;2

Braun, J., Chéry, J., Poliakov, A., Mainprice, D., Vauchez, A., Tomassi, A., & Daignières, M. (1999). A simple parameterization of strain localization in the ductile regime due to grain size reduction: A case study for olivine. *Journal of Geophysical Research*, *104*(B11), 25,167–25,181. https://doi.org/10.1029/1999JB900214

Brown, M., & Solar, G. S. (1999). The mechanism of ascent and emplacement of granite magma during transpression: A syntectonic granite paradigm. *Tectonophysics*, *312*(1), 1–33. https://doi.org/10.1016/S0040-1951(99)00169-9

Bunge, H.-J. (1982). *Texture analysis in materials science: Mathematical methods*. Berlin: Butterworths & Co.

Cannat, M. (1993). Emplacement of mantle rocks in the seafloor at mid-ocean ridges. *Journal of Geophysical Research*, *98*(B3), 4163–4172. https://doi.org/10.1029/92JB02221

Cannat, M., & Sauter, D. (2009). Assessing the conditions of continental breakup at magma-poor rifted margins: What can we learn from slow spreading mid-ocean ridges? *Comptes Rendus Geoscience*, *341*(5), 406–427. https://doi.org/10.1016/J.CRTE.2009.01.005

Cannat, M., Sauter, D., Lavier, L., Bickert, M., Momoh, E., & Leroy, S. (2019). On spreading modes and magma supply at slow and ultraslow mid-ocean ridges. *Earth and Planetary Science Letters*, *519*, 223–233. https://doi.org/10.1016/J.EPSL.2019.05.012

Cao, S., Liu, J., & Leiss, B. (2010). Orientation-related deformation mechanisms of naturally deformed amphibole in amphibolite mylonites from the Diancang Shan, SW Yunnan, China. *Journal of Structural Geology*, *32*(5), 606–622. https://doi.org/10.1016/J.JSG.2010.03.012

Chen, Y., & Morgan, W. J. (1990). A nonlinear rheology model for mid-ocean ridge axis topography. *Journal of Geophysical Research*, *95*(B11), 17583. https://doi.org/10.1029/JB095iB11p17583

Cipriani, A., Bonatti, E., Seyler, M., Brueckner, H. K., Brunelli, D., Dallai, L., et al. (2009). A 19 to 17 Ma amagmatic extension event at the Mid-Atlantic Ridge: Ultramafic mylonites from the Vema Lithospheric Section. *Geochemistry, Geophysics, Geosystems*, *10*, Q10011. https://doi.org/10.1029/2009GC002534

Debret, B., Nicollet, C., Andreani, M., Schwartz, S., & Godard, M. (2013). Three steps of serpentinization in an eclogitized oceanic serpentinization front (Lanzo Massif–Western Alps). *Journal of Metamorphic Geology*, *31*(2), 165–186. https://doi.org/10.1111/jmg.12008

Decitre, S., Deloule, E., Reisberg, L., James, R., Agrinier, P., & Mével, C. (2002). Behavior of Li and its isotopes during serpentinization of oceanic peridotites. *Geochemistry, Geophysics, Geosystems*, *3*(1), 1007. https://doi.org/10.1029/2001GC000178

Díaz Aspiroz, M., Lloyd, G. E., & Fernández, C. (2007). Development of lattice preferred orientation in clinoamphiboles deformed under low-pressure metamorphic conditions. A SEM/EBSD study of metabasites from the Aracena metamorphic belt (SW Spain). *Journal of Structural Geology*, *29*(4), 629–645. https://doi.org/10.1016/J.JSG.2006.10.010

Dijkstra, A. H., Drury, M. R., & Frijhoff, R. M. (2002). Microstructures and lattice fabrics in the Hilti mantle section (Oman Ophiolite): Evidence for shear localization and melt weakening in the crust–mantle transition zone? *Journal of Geophysical Research*, *107*(B11), 2270. https://doi.org/10.1029/2001JB000458

Dollinger, G., & Blacic, J. D. (1975). Deformation mechanisms in experimentally and naturally deformed amphiboles. *Earth and Planetary Science Letters*, *26*(3), 409–416. https://doi.org/10.1016/0012-821X(75)90016-3

Drury, M. R., & Urai, J. L. (1990). Deformation-related recrystallization processes. *Tectonophysics*, *172*(3–4), 235–253. https://doi.org/10.1016/0040-1951(90)90033-5

Durham, W. B., & Goetze, C. (1977). Plastic flow of oriented single crystals of olivine: 1. Mechanical data. *Journal of Geophysical Research*, *82*(36), 5737–5753. https://doi.org/10.1029/JB082i036p05737

Evans, B. (1982). Amphiboles in metamorphosed ultramafic rocks. In D. R. Veblen & P. H. Ribble (Eds.), *Amphiboles: Petrology and experimental phase relations*, *Reviews in Mineralogy* (Vol. 9B, pp. 98–113). Washington, DC: Mineralogical Society of America.

Evans, B., Renner, J., & Hirth, G. (2001). A few remarks on the kinetics of static grain growth in rocks. *International Journal of Earth Sciences*, *90*(1), 88–103. https://doi.org/10.1007/s005310000150

Früh-Green, G. L., Plas, A., & Lécuyer, C. (1996). Petrologic and stable isotope constraints on hydrothermal alteration and serpentinization of the EPR shallow mantle at Hess Deep (site 895). *Proceeding of the Ocean Drilling Program, Scientific Results*, *147*(14).

Fumagalli, P., Borghini, G., Rampone, E., & Poli, S. (2017). Experimental calibration of Forsterite–Anorthite–Ca-Tschermak–Enstatite (FACE) geobarometer for mantle peridotites. *Contributions to Mineralogy and Petrology*, *172*(6), 38. https://doi.org/10.1007/s00410-017-1352-2

Fumagalli, P., Zanchetta, S., & Poli, S. (2009). Alkali in phlogopite and amphibole and their effects on phase relations in metasomatized peridotites: A high-pressure study. *Contributions to Mineralogy and Petrology*, *158*(6), 723–737. https://doi.org/10.1007/s00410-009-0407-4

Fusseis, F., Regenauer-Lieb, K., Liu, J., Hough, R. M., & De Carlo, F. (2009). Creep cavitation can establish a dynamic granular fluid pump in ductile shear zones. *Nature*, *459*(7249), 974–977. https://doi.org/10.1038/nature08051

Gillard, M., Tugend, J., Müntener, O., Manatschal, G., Karner, G. D., Autin, J., et al. (2019). The role of serpentinization and magmatism in the formation of decoupling interfaces at magma-poor rifted margins. *Earth-Science Reviews*, *196*, 102882. https://doi.org/10.1016/J.EARSCIREV.2019.102882

Gregory, R. T., & Taylor, H. P. Jr. (1981). An oxygen isotope profile in a section of Cretaceous oceanic crust, Samail Ophiolite, Oman: Evidence for $\delta^{18}O$ buffering of the oceans by deep (>5 km) seawater-hydrothermal circulation at mid-ocean ridges. *Journal of Geophysical Research*, *86*(B4), 2737–2755. https://doi.org/10.1029/JB086iB04p02737

Grevemeyer, I., Hayman, N. W., Lange, D., Peirce, C., Papenberg, C., van Avendonk, H. J. A., et al. (2019). Constraining the maximum depth of brittle deformation at slow- and ultraslow-spreading ridges using microseismicity. *Geology*, *47*(11), 1069–1073. https://doi.org/10.1130/G46577.1

Hellebrand, E., Snow, J. E., Hoppe, P., & Hofmann, A. W. (2002). Garnet-field melting and late-stage refertilization in "residual" abyssal peridotites from the Central Indian Ridge. *Journal of Petrology*, *43*(12), 2305–2338. https://doi.org/10.1093/petrology/43.12.2305

Henry, H., Tilhac, R., Griffin, W. L., O'Reilly, S. Y., Satsukawa, T., Kaczmarek, M.-A., et al. (2017). Deformation of mantle pyroxenites provides clues to geodynamic processes in subduction zones: Case study of the Cabo Ortegal Complex, Spain. *Earth and Planetary Science Letters*, *472*, 174–185. https://doi.org/10.1016/J.EPSL.2017.05.028

Hidas, K., Garrido, C. J., Tommasi, A., Padrón-Navarta, J. A., Thielmann, M., Konc, Z., et al. (2013). Strain localization in pyroxenite by reaction-enhanced softening in the shallow subcontinental lithospheric mantle. *Journal of Petrology*, *54*(10), 1997–2031. https://doi.org/10.1093/petrology/egt039

Hidas, K., Tommasi, A., Garrido, C. J., Padrón-Navarta, J. A., Mainprice, D., Vauchez, A., et al. (2016). Fluid-assisted strain localization in the shallow subcontinental lithospheric mantle. *Lithos*, *262*, 636–650. https://doi.org/10.1016/j.lithos.2016.07.038

Hirth, G., & Kohlstedt, D. L. (1995). Experimental constraints on the dynamics of the partially molten upper mantle: 2. Deformation in the dislocation creep regime. *Journal of Geophysical Research*, *100*(B8), 15,441–15,449. https://doi.org/10.1029/95JB01292

Holtzman, B. K., Groebner, N. J., Zimmerman, M. E., Ginsberg, S. B., & Kohlstedt, D. L. (2003). Stress-driven melt segregation in partially molten rocks. *Geochemistry, Geophysics, Geosystems*, *4*(5), 8607. https://doi.org/10.1029/2001GC000258

Holtzman, B. K., & Kohlstedt, D. L. (2007). Stress-driven melt segregation and strain partitioning in partially molten rocks: Effects of stress and strain. *Journal of Petrology*, *48*(12), 2379–2406. https://doi.org/10.1093/petrology/egm065

Ildefonse, B., Blackman, D. K., John, B. E., Ohara, Y., Miller, D. J., & MacLeod, C. J. (2007). Oceanic core complexes and crustal accretion at slow-spreading ridges. *Geology*, *35*(7), 623. https://doi.org/10.1130/G23531A.1

Janecky, D. R., & Seyfried, W. E. (1986). Hydrothermal serpentinization of peridotite within the oceanic crust: Experimental investigations of mineralogy and major element chemistry. *Geochimica et Cosmochimica Acta*, *50*(7), 1357–1378. https://doi.org/10.1016/0016-7037(86)90311-X

Jaroslow, G. E., Hirth, G., & Dick, H. J. B. (1996). Abyssal peridotite mylonites: Implications for grain-size sensitive flow and strain localization in the oceanic lithosphere. *Tectonophysics*, *256*(1–4), 17–37. https://doi.org/10.1016/0040-1951(95)00163-8

Jollands, M. C., & Müntener, O. (2019). Testing orthopyroxene diffusion chronometry on rocks from the Lanzo Massif (Italian Alps). *Journal of Geophysical Research: Solid Earth*, *124*, 7822–7841. https://doi.org/10.1029/2018JB016963

Jung, H., & Karato, S. I. (2001). Water-induced fabric transitions in olivine. *Science*, *293*(5534), 1460–1463. https://doi.org/10.1126/science.1062235

Jung, H., Park, M., Jung, S., & Lee, J. (2010). Lattice preferred orientation, water content, and seismic anisotropy of orthopyroxene. *Journal of Earth Science*, *21*(5), 555–568. https://doi.org/10.1007/s12583-010-0118-9

Kaczmarek, M.-A. (2007). Melt migration and deformation in the upper mantle: An example of the Lanzo peridotite massif (Western Alps, Italy) (Doctoral disseration). Retrieved from Rero doc (https://doc.rero.ch/record/8140/files/these_KaczmarekM.pdf). Université de Neuchâtel.

Kaczmarek, M.-A., & Müntener, O. (2008). Juxtaposition of melt impregnation and high-temperature shear zones in the upper mantle; field and petrological constraints from the Lanzo peridotite (Northern Italy). *Journal of Petrology*, *49*(12), 2187–2220. https://doi.org/10.1093/petrology/egn065

Kaczmarek, M.-A., & Tommasi, A. (2011). Anatomy of an extensional shear zone in the mantle, Lanzo massif, Italy. *Geochemistry, Geophysics, Geosystems*, *12*, Q0AG06. https://doi.org/10.1029/2011GC003627

Karato, S., Jung, H., Katayama, I., & Skemer, P. (2008). Geodynamic significance of seismic anisotropy of the upper mantle: New insights from laboratory studies. *Annual Review of Earth and Planetary Sciences*, *36*(1), 59–95. https://doi.org/10.1146/annurev.earth.36.031207.124120

Katayama, I., Jung, H., & Karato, S. I. (2004). New type of olivine fabric from deformation experiments at modest water content and low stress. *Geology*, *32*(12), 1045–1048. https://doi.org/10.1130/G20805.1

Kelemen, P. B., Shimizu, N., & Salters, V. J. M. (1995). Extraction of mid-ocean-ridge basalt from the upwelling mantle by focused flow of melt in dunite channels. *Nature*, *375*(6534), 747–753. https://doi.org/10.1038/375747a0

Kohlstedt, D. L., & Holtzman, B. K. (2009). Shearing melt out of the Earth: An experimentalist's perspective on the influence of deformation on melt extraction. *Annual Review of Earth and Planetary Sciences*, *37*(1), 561–593. https://doi.org/10.1146/annurev.earth.031208.100104

Kullerud, K., & Erambert, M. (1999). Cl-scapolite, Cl-amphibole, and plagioclase equilibria in ductile shear zones at Nusfjord, Lofoten, Norway: Implications for fluid compositional evolution during fluid-mineral interaction in the deep crust. *Geochimica et Cosmochimica Acta*, *63*(22), 3829–3844. https://doi.org/10.1016/S0016-7037(99)00150-7

Lacroix, B., & Vennemann, T. (2015). Empirical calibration of the oxygen isotope fractionation between quartz and Fe–Mg-chlorite. *Geochimica et Cosmochimica Acta*, *149*, 21–31. https://doi.org/10.1016/J.GCA.2014.10.031

Lagabrielle, Y., & Lemoine, M. (1997). Alpine, Corsican and Apennine ophiolites: The slow-spreading ridge model. *Comptes Rendus de l'Académie Des Sciences—Series IIA—Earth and Planetary Science*, *325*(12), 909–920. https://doi.org/10.1016/S1251-8050(97)82369-5

Le Roux, V., Tommasi, A., & Vauchez, A. (2008). Feedback between melt percolation and deformation in an exhumed lithosphere–asthenosphere boundary. *Earth and Planetary Science Letters*, *274*(3–4), 401–413. https://doi.org/10.1016/J.EPSL.2008.07.053

Leake, B. E., Woolley, A. R., Arps, C. E. S., Birch, W. D., Gilbert, M. C., Grice, J. D., et al. (1997). Nomenclature of amphiboles: Report of the Subcommittee on Amphiboles of the International Mineralogical Association, Commission on New Minerals and Mineral Names. *American Mineralogist*, *61*(405), 295–310. https://doi.org/10.1180/minmag.1997.061.405.13

Lemoine, M., Tricart, P., & Boillot, G. (1987). Ultramafic and gabbroic ocean floor of the Ligurian Tethys (Alps, Corsica, Apennines): In search of a genetic imodel. *Geology*, *15*(7), 622. https://doi.org/10.1130/0091-7613(1987)15<622:UAGOFO>2.0.CO;2

Linckens, J., Herwegh, M., Müntener, O., & Mercolli, I. (2011). Evolution of a polymineralic mantle shear zone and the role of second phases in the localization of deformation. *Journal of Geophysical Research*, *116*, B06210. https://doi.org/10.1029/2010JB008119

Liu, Y. C. (1999). Crystallographic preferred orientation and slip system of amphibole in the Florence shear zone, central Australia. *Journal of Mineralogy and Petrology*, *19*, 1–7.

Markl, G., & Bucher, K. (1998). Composition of fluids in the lower crust inferred from metamorphic salt in lower crustal rocks. *Nature*, *391*(6669), 781–783. https://doi.org/10.1038/35836

McGuire, J. J., Collins, J. A., Gouédard, P., Roland, E., Lizarralde, D., Boettcher, M. S., et al. (2012). Variations in earthquake rupture properties along the Gofar transform fault, East Pacific Rise. *Nature Geoscience*, *5*(5), 336–341. https://doi.org/10.1038/ngeo1454

McKenzie, D., Jackson, J., & Priestley, K. (2005). Thermal structure of oceanic and continental lithosphere. *Earth and Planetary Science Letters*, *233*(3–4), 337–349. https://doi.org/10.1016/J.EPSL.2005.02.005

Melson, W. G., Hart, S. R., & Thompson, G. (1972). St. Paul's rocks, equatorial Atlantic: Petrogenesis, radiometric ages, and implications on sea-floor spreading. In R. Shagam, et al. (Eds.), *Studies in Earth and space sciences* (Vol. 132, pp. 241–272). America: Geological Society. https://doi.org/10.1130/MEM132-p241

Mével, C. (2003). Serpentinization of abyssal peridotites at mid-ocean ridges. *Comptes Rendus Geoscience*, *335*, 825–852. https://doi.org/10.1016/j.crte.2003.08.006

Minshull, T. A. (2009). Geophysical characterisation of the ocean-continent transition at magma-poor rifted margins. *Comptes Rendus Geoscience*, *341*(5), 382–393. https://doi.org/10.1016/j.crte.2008.09.003

Minshull, T. A., Muller, M. R., Robinson, C. J., White, R. S., & Bickle, M. J. (1998). Is the oceanic Moho a serpentinization front? *Geological Society, London, Special Publications*, *148*(1), 71–80. https://doi.org/10.1144/GSL.SP.1998.148.01.05

Muehlenbachs, K. (1987). Oxygen isotope exchange during weathering and low temperature alteration. In T. K. Kyser (Ed.), *Short course in stable isotope geochemistry of low temperature fluids* (Vol. 13, pp. 337–445). Toronto, Ontario: Mineralogical Association of Canada.

Newman, J., Lamb, W. M., Drury, M. R., & Vissers, R. L. (1999). Deformation processes in a peridotite shear zone: Reaction-softening by an H_2O-deficient, continuous net transfer reaction. *Tectonophysics*, *303*(1–4), 193–222. https://doi.org/10.1016/S0040-1951(98)00259-5

Nicolas, A. (1974). Mise en place des péridotites de Lanzo (Alpes piémontaises) Relation avec tectonique et métamorphisme alpins: conséquences géodynamiques. *Schweizerische Mineralogische und Petrographische Mitteilungen*, *54*, 449–460.

Niida, K., & Green, D. H. (1999). Stability and chemical composition of pargasitic amphibole in MORB pyrolite under upper mantle conditions. *Contributions to Mineralogy and Petrology*, *135*(1), 18–40. https://doi.org/10.1007/s004100050495

Palasse, L. N., Vissers, R. L. M., Paulssen, H., Basu, A. R., & Drury, M. R. (2012). Microstructural and seismic properties of the upper mantle underneath a rifted continental terrane (Baja California): An example of sub-crustal mechanical asthenosphere? *Earth and Planetary Science Letters*, *345–348*, 60–71. https://doi.org/10.1016/j.epsl.2012.06.042

Parnell-Turner, R., Sohn, R. A., Peirce, C., Reston, T. J., MacLeod, C. J., Searle, R. C., & Simão, N. M. (2017). Oceanic detachment faults generate compression in extension. *Geology*, *45*(10), 923–926. https://doi.org/10.1130/G39232.1

Pelletier, L., & Müntener, O. (2006). High-pressure metamorphism of the Lanzo peridotite and its oceanic cover, and some consequences for the Sesia–Lanzo zone (northwestern Italian Alps). *Lithos*, *90*(1–2), 111–130. https://doi.org/10.1016/J.LITHOS.2006.01.006

Picazo, S., Cannat, M., Delacour, A., Escartín, J., Rouméjon, S., & Silantyev, S. (2012). Deformation associated with the denudation of mantle-derived rocks at the Mid-Atlantic Ridge 13°–15°N: The role of magmatic injections and hydrothermal alteration. *Geochemistry, Geophysics, Geosystems*, *13*, Q04G09. https://doi.org/10.1029/2012GC004121

Platt, J. P., & Vissers, R. L. M. (1980). Extensional structures in anisotropic rocks. *Journal of Structural Geology*, *2*(4), 397–410. https://doi.org/10.1016/0191-8141(80)90002-4

Pognante, U. (1989). Lawsonite, blueschist and eclogite formation in the southern Sesia zone (western Alps, Italy). *European Journal of Mineralogy*, *1*(1), 89–104. https://doi.org/10.1127/ejm/01/1/0089

Pognante, U., Rösli, U., & Toscani, L. (1985). Petrology of ultramafic and mafic rocks from the Lanzo peridotite body (Western Alps). *Lithos*, *18*, 201–214. https://doi.org/10.1016/0024-4937(85)90025-8

Précigout, J., & Gueydan, F. (2009). Mantle weakening and strain localization: Implications for the long-term strength of the continental lithosphere. *Geology*, *37*(2), 147–150. https://doi.org/10.1130/G25239A.1

Précigout, J., Prigent, C., Palasse, L., & Pochon, A. (2017). Water pumping in mantle shear zones. *Nature Communications*, *8*, 15736. https://doi.org/10.1038/ncomms15736

Prigent, C., Warren, J. M. M., Kohli, A. H. H., & Teyssier, C. (2020). Fracture-mediated deep seawater flow and mantle hydration on oceanic transform faults. *Earth and Planetary Science Letters*, *532*, 115988.

Regenauer-Lieb, K., & Yuen, D. A. (2003). Modeling shear zones in geological and planetary sciences: Solid- and fluid-thermal–mechanical approaches. *Earth-Science Reviews*, *63*(3–4), 295–349. https://doi.org/10.1016/S0012-8252(03)00038-2

Rooney, T. P., Riecker, R. E., & Gavasci, A. T. (1975). Hornblende deformation features. *Geology*, *3*(7), 364. https://doi.org/10.1130/0091-7613(1975)3<364:HDF>2.0.CO;2

Rosenberg, C. L., & Handy, M. R. (2000). Syntectonic melt pathways during simple shearing of a partially molten rock analogue (Norcamphor-Benzamide). *Journal of Geophysical Research*, *105*(B2), 3135–3149. https://doi.org/10.1029/1999JB900371

Schlindwein, V., & Schmid, F. (2016). Mid-ocean-ridge seismicity reveals extreme types of ocean lithosphere. *Nature*, *535*(7611), 276–279. https://doi.org/10.1038/nature18277

Seyler, M., & Bonatti, E. (1997). Regional-scale melt-rock interaction in lherzolitic mantle in the Romanche Fracture Zone (Atlantic Ocean). *Earth and Planetary Science Letters*, *146*(1–2), 273–287. https://doi.org/10.1016/S0012-821X(96)00220-8

Sharp, Z. D. (1990). A laser-based microanalytical method for the in situ determination of oxygen isotope ratios of silicates and oxides. *Geochimica et Cosmochimica Acta*, *54*(5), 1353–1357. https://doi.org/10.1016/0016-7037(90)90160-M

Sibson, R. H., Moore, J. M. M., & Rankin, A. H. (1975). Seismic pumping—A hydrothermal fluid transport mechanism. *Journal of the Geological Society*, *131*(6), 653–659. https://doi.org/10.1144/gsjgs.131.6.0653

Skelton, A., Whitmarsh, R., Arghe, F., Crill, P., & Koyi, H. (2005). Constraining the rate and extent of mantle serpentinization from seismic and petrological data: Implications for chemosynthesis and tectonic processes. *Geofluids*, *5*(3), 153–164. https://doi.org/10.1111/j.1468-8123.2005.00111.x

Skemer, P., Katayama, I., Jiang, Z., & Karato, S. (2005). The misorientation index: Development of a new method for calculating the strength of lattice-preferred orientation. *Tectonophysics*, *411*(1–4), 157–167. https://doi.org/10.1016/J.TECTO.2005.08.023

Soustelle, V., Tommasi, A., Bodinier, J. L., Garrido, C. J., & Vauchez, A. (2009). Deformation and reactive melt transport in the mantle lithosphere above a large-scale partial melting domain: The Ronda Peridotite Massif, Southern Spain. *Journal of Petrology*, *50*(7), 1235–1266. https://doi.org/10.1093/petrology/egp032

Spalla, M. I., De Maria, L., Gosso, G., Miletto, M., & Pognante, U. (1983). Deformazione e metamorfismo della Zona Sesia-Lanzo meridionale al contatto con la falda piemontese e con il massiccio di Lanzo, Alpi occidentali. *Memorie Della Società Geologica Italiana*, *26*, 499–514.

Sundberg, M., & Cooper, R. F. (2008). Crystallographic preferred orientation produced by diffusional creep of harzburgite: Effects of chemical interactions among phases during plastic flow. *Journal of Geophysical Research*, *113*, B12208. https://doi.org/10.1029/2008JB005618

Takei, Y. (2005). Deformation-induced grain boundary wetting and its effects on the acoustic and rheological properties of partially molten rock analogue. *Journal of Geophysical Research*, *110*, B12203. https://doi.org/10.1029/2005JB003801

Talbi, E. L. H., & Gauthier-Lafaye, C. F. (1999). Petrology, isotope geochemistry and chemical budgets of oceanic gabbros-seawater interactions in the Equatorial Atlantic. *Contributions to Mineralogy and Petrology*, *137*, 246–266.

Tilhac, R., Ceuleneer, G., Griffin, W. L., O'Reilly, S. Y., Pearson, N. J., Benoit, M., et al. (2016). Primitive arc magmatism and delamination: Petrology and geochemistry of pyroxenites from the Cabo Ortegal Complex, Spain. *Journal of Petrology*, *57*(10), 1921–1954. https://doi.org/10.1093/petrology/egw064

Tommasi, A., Knoll, M., Vauchez, A., Signorelli, J. W., Thoraval, C., & Logé, R. (2009). Structural reactivation in plate tectonics controlled by olivine crystal anisotropy. *Nature Geoscience*, *2*(6), 423–427. https://doi.org/10.1038/ngeo528

Tommasi, A., Vauchez, A., Femandes, L. A. D., & Porcher, C. C. (1994). Magma-assisted strain localization in an orogen-parallel transcurrent shear zone of southern Brazil. *Tectonics*, *13*(2), 421–437. https://doi.org/10.1029/93TC03319

Tucholke, B. E., Fujioka, K., Ishihara, T., Hirth, G., & Kinoshita, M. (2001). Submersible study of an oceanic megamullion in the central North Atlantic. *Journal of Geophysical Research*, *106*(B8), 16,145–16,161. https://doi.org/10.1029/2001JB000373

Tucholke, B. E., Lin, J., & Kleinrock, M. C. (1998). Megamullions and mullion structure defining oceanic metamorphic core complexes on the Mid-Atlantic Ridge. *Journal of Geophysical Research*, *103*(B5), 9857–9866. https://doi.org/10.1029/98JB00167

Turner, F. J., Heard, H., & Griggs, D. T. (1960). Experimental deformation of enstatite and accompanying inversion to clinoenstatite. In *XXI International Geological Congress Copenhagen* (pp. 399–408).

Ulmer, P., & Trommsdorff, V. (1999). Phase relations of hydrous mantle subducting to 300 km. In Y. Frei, C. M. Bertka, B. O. Mysen (Eds.), *Mantle petrology: Field observations and high pressure experimentation. A tribute to Francis R. (Joe) Boyd*, *Special Publication 6* (pp. 259–281). Stony Brook, NY: The Geochemical Society.

Vernon, R. H. (2018). *A practical guide to rock microstructure*. Cambridge: Cambridge University Press. https://doi.org/10.1017/9781108654609

Vissers, R. L. M., Drury, M. R., Hoogerduijn Strating, E. H., Spiers, C. J., & van der Wal, D. (1995). Mantle shear zones and their effect on lithosphere strength during continental breakup. *Tectonophysics*, *249*(3–4), 155–171. https://doi.org/10.1016/0040-1951(95)00033-J

Vitale Brovarone, A., Martinez, I., Elmaleh, A., Compagnoni, R., Chaduteau, C., Ferraris, C., & Esteve, I. (2017). Massive production of abiotic methane during subduction evidenced in metamorphosed ophicarbonates from the Italian Alps. *Nature Communications*, *8*(1), 14134. https://doi.org/10.1038/ncomms14134

Wark, D. A., & Watson, E. B. (2000). Effect of grain size on the distribution and transport of deep-seated fluids and melts. *Geophysical Research Letters*, *27*(14), 2029–2032. https://doi.org/10.1029/2000GL011503

Warren, J. M., & Hirth, G. (2006). Grain size sensitive deformation mechanisms in naturally deformed peridotites. *Earth and Planetary Science Letters*, *248*(1–2), 438–450. https://doi.org/10.1016/J.EPSL.2006.06.006

Yu, Z., Li, J., Niu, X., Rawlinson, N., Ruan, A., Wang, W., et al. (2018). Lithospheric structure and tectonic processes constrained by microearthquake activity at the central ultraslow-spreading Southwest Indian Ridge (49.2° to 50.8°E). *Journal of Geophysical Research: Solid Earth*, *123*, 6247–6262. https://doi.org/10.1029/2017JB015367